

NuSTAR observation of LS 5039

IGOR VOLKOV,¹ OLEG KARGALTSEV,¹ GEORGE YOUNES,¹ JEREMY HARE,^{2,*} AND GEORGE PAVLOV³

¹*The George Washington University, Department of Physics, 725 21st St NW, Washington, DC 20052*

²*NASA Goddard Space Flight Center, Greenbelt MD, 20771, USA*

³*Pennsylvania State University, Department of Astronomy & Astrophysics, 525 Davey Laboratory, University Park, PA 16802*

ABSTRACT

LS 5039 is a high-mass γ -ray binary hosting a compact object of unknown type. *NuSTAR* observed LS 5039 during the entire 3.9 day binary period. We performed a periodic signal search up to 1000 Hz which did not produce credible period candidates. We do see the 9.05 s period candidate, originally reported by Yoneda et al. (2020) using the same data, in the Fourier power spectrum, but we find that the statistical significance of this feature is too low to claim it as a real detection. We also did not find significant bursts or quasi-periodic variability. The modulation with the orbital period is clearly seen and remains unchanged over a decade timescale when compared to the earlier *Suzaku* light curve. The joint analysis of the *NuSTAR* and *Suzaku* XIS data shows that the 0.7–70 keV spectrum can be satisfactorily described by a single absorbed power-law model with no evidence of cutoff at higher energies. The slope of the spectrum anti-correlates with the flux during the binary orbit. Therefore, if LS 5039 hosts a young neutron star, its X-ray pulsations appear to be outshined by the intrabinary shock emission. The lack of spectral lines and/or an exponential cutoff at higher energies suggests that the putative neutron star is not actively accreting. Although a black hole scenario still remains a possibility, the lack of variability or Fe $K\alpha$ lines, which typically accompany accretion, makes it less likely.

Keywords: X-rays: individual (LS 5039) — X-rays: binaries — gamma rays: stars

1. INTRODUCTION

High-mass γ -ray binaries (HMGBs) consist of a compact object, either a neutron star (NS) or black hole (BH), orbiting a hot, massive O or B type star. The number of known HMGBs has been increasing in recent years (Paredes, & Bordas 2019). However, in all but two HMGBs (LS 2883/B1259–63 and MT91 213/TeV J2031+4130), which host young pulsars, the nature of the compact object remains unknown. Two scenarios for high-energy emission of HMGBs are usually discussed: (1) interaction of the pulsar wind with the wind of the massive donor star leading to the formation of an intrabinary shock, or (2) jets powered by accretion onto a compact object (likely a BH). All HMGBs that have been observed with VLBI exhibit extended radio emission on millisecond scales, which can be attributed to either a pulsar-wind nebula or to jets produced by

accretion onto a BH (i.e., the classical microquasar scenario).

X-ray observations can provide important information for understanding the nature of HMGBs. Therefore, these objects have been extensively observed in soft and hard X-rays. In particular, *NuSTAR* observed LS 2883 (Chernyakova et al. 2015), MT91 213 (Li et al. 2017), 1FGL J1018.6–5856 (An et al. 2015), HESS J0632+057 (Prado et al. 2019; Archer et al. 2020), LSI +61°303 (Massi et al. 2020), and LMC P3 (Coley et al. 2020). All of these HMGBs were also observed in soft X-rays with *XMM-Newton*, *Swift*, *Suzaku*, and *Chandra* (see e.g., Takahashi et al. 2009; Dubus 2013; Kargaltsev et al. 2014). In all cases, the X-ray spectra appear to be consistent with featureless power-laws (PLs) with photon indices $\Gamma \simeq 1.3 - 2$. Joint fits to the soft X-ray and hard X-ray spectra provide no evidence of a spectral cut-off in the *NuSTAR* band. No periodicity associated with the compact object spin has been found in any of the X-ray data (including two systems with known radio pulsars – LS 2883 with PSR B1259–63 and MT91 213

kargaltsev@email.gwu.edu

* NASA Postdoctoral Program Fellow

with PSR J2032+4127). Using NuSTAR data, An et al. (2015) and Archer et al. (2020) found no short-term variability, quasi-periodic oscillations, red noise, or any other temporal or spectral evidence of accretion in 1FGL J1018.6–5856 and HESS J0632+057, respectively.

LS 5039, discovered by Marti et al. (1998), is a binary at a distance $d = 2.9 \pm 0.8$ kpc composed of a massive ($M_* = 23 M_\odot$) O6.5V(f) type star ($V = 11.2$ mag) and a compact object with a poorly constrained mass, $\sim (1-4)M_\odot$. The compact object orbits the star with a period $P_{\text{orb}} \simeq 3.9$ days, which is the shortest orbital period among all HMGBs. The binary orbit inclination angle is $i \sim 30^\circ$ (Casares et al. 2005; Sarty et al. 2011). Radio observations have shown a persistent (over many binary periods) AU-scale asymmetric extension around LS 5039 whose morphology varies with orbital phase (Moldón et al. 2012). Initially the extension was interpreted as jets from an accreting compact object, which led to a “microquasar” classification (Paredes et al. 2000). However, more recently Moldón et al. (2012) attributed the varying extended radio morphology to a pulsar wind nebula whose shape varies due to the interaction with the wind of the massive star. Overall, the debate over whether the compact object is an accreting BH or a pulsar interacting with its surroundings and producing an extended nebula resembling “jets” is still ongoing (see e.g., Dubus 2015).

Obviously, the most direct evidence of LS 5039 containing a pulsar would be the detection of pulsations. However, among all HMGBs radio pulsations have only been detected in LS 2883 and MT91 213 (Camilo et al. 2009; Shannon et al. 2014). Even if LS 5039 hosts a pulsar, the non-detection of radio pulsations is not surprising because of the tight orbit and correspondingly large optical depth to free-free absorption (Dubus 2006). Therefore, searching for pulsations in X-rays may be a more promising approach for LS 5039 than for the other HMGBs.

Pulsations have been searched for in previous X-ray observations of LS 5039. For instance, Rea et al. (2011) found no periodicity in the CXO observation of LS 5039. However, Yoneda et al. (2020), hereafter Y+20, have recently reported the detection of a period $P \approx 8.96$ s in the Suzaku HXD data from 2007, and a potential counterpart at $P \approx 9.05$ s in the NuSTAR data from 2016 (the same data we analyze below), at photon energies above 10 keV. The difference in the periods implies a fast spin-down, suggesting that the compact object in LS 5039 could be a magnetar (i.e., a NS with a very high magnetic field; Kaspi & Beloborodov 2017). The statistical significance of this result is, however, questionable, as discussed below.

The shape of the hard X-ray spectrum can also provide critical information about the nature of the compact object. For instance, some NSs in accreting HMXBs show cyclotron resonant scattering features in the range of about 10–100 keV and many of them have exponential cutoffs around a few tens of keV (e.g., Coburn et al. 2002). Such spectral characteristics are very efficiently detected with NuSTAR (see e.g., Fürst et al. 2014; Tsygankov et al. 2016). LS 5039’s spectrum was studied in the 0.01–10 MeV range with INTEGRAL, RXTE, Suzaku, and CGRO. Most of these measurements suggest a relatively soft high-energy spectrum ($\Gamma \approx 2$), while the Suzaku HXD spectrum is more consistent with a simple extrapolation of the $\Gamma = 1.4-1.6$ PL spectrum measured below 10 keV with CXO, XMM-Newton, and Suzaku XIS (Takahashi et al. 2009).

Of all known HMGBs, LS 5039 has the shortest orbital period. This prompted us to carry out NuSTAR observations of LS 5039 over the entire orbital period to obtain a complete spectral and temporal portrait of this HMGB. Additionally, we used archival Suzaku XIS observations that also cover the full binary period and extend spectral coverage to lower energies. In Section 2 we describe the NuSTAR and Suzaku observations and data reduction procedures. In Section 3 we describe the binary orbit corrections to the arrival times caused by the compact object’s motion around its massive companion and present the results of the periodicity and variability search. In Section 4 we present the spectrum of LS 5039 and the results of spectral fitting as a function of the orbital phase. We discuss our findings and conclude with a brief summary in Section 5.

2. OBSERVATIONS AND DATA REDUCTION

The Nuclear Spectroscopic Telescope Array (NuSTAR, Harrison et al. 2013) consists of two similar modules, FPMA and FPMB, operating in the energy range 3–79 keV. The NuSTAR observation of LS 5039 (ObsID 30201034002) started on 2016 September 1 (MJD 57632.0972) and lasted for $T_{\text{obs}} \approx 345$ ks $\approx 1.024P_{\text{orb}}$ (≈ 60 consecutive NuSTAR orbits). We processed the data using the NuSTAR Data Analysis Software, `nustardas` ver. 1.8.0. The photon arrival times were corrected to the solar system barycenter using the `barycorr` tool¹ and the latest clock correction file². The timing accuracy of NuSTAR is expected to be 65 μ s, on

¹ See <https://heasarc.gsfc.nasa.gov/ftools/caldb/help/barycorr.html>.

² `nuCclock20100101v110.fits.gz` http://nustarsoc.caltech.edu/NuSTAR_Public/NuSTAROperationSite/clockfile.php

average (Bachetti et al. 2021). We reduced the data using the `nuproducts` task and HEASOFT ver. 6.22.1.

For spectral analysis and binary lightcurves we used the flags `-saacalc=2 --saamode=optimized --tentacle=yes` to correct for enhanced background activity visible at the edges of the good time intervals (GTIs) immediately before entering the SAA. This resulted in a total GTI of about 166 ks. We extracted source events from the 60'' radius circle around the source position, which maximized the S/N ratio. Background events are extracted from an annulus around the source position with the inner and outer radii of 120'' and 200''.

To extend the spectral analysis to lower energies, we used archival *Suzaku* data. *Suzaku* observed LS 5039 between 2007 September 9 and 2007 September 15, with a total scientific exposure time of ≈ 203 ks (obsID 402015010). The observation, originally reported by Takahashi et al. (2009), provided coverage of about 1.5 orbits of the LS 5039 binary. In the soft X-ray energy band (0.3–12 keV), *Suzaku* had four X-ray telescopes (Serlemitsos et al. 2007) each with its own focal plane CCD camera (X-ray Imaging Spectrometer; XIS; Koyama et al. 2007) having an $18' \times 18'$ field-of-view. The XIS2 camera was turned off in November 2006 due to an anomaly and is not used in our analysis. The XIS0 and XIS3 detectors use front-illuminated CCDs, while the XIS1 has a back-illuminated CCD.

We used HEASOFT ver. 6.25 for *Suzaku* data reduction. The data were reprocessed using the `aepipeline` script and were reduced following the standard procedures³. The source spectra and light curves were extracted from a 3' radius circle centered on the source position, while the background spectra and light curves were extracted from a 3' circle placed 7.5 south of the source in each of the three XIS images. The response matrix and ancillary response file were made using the `xisrmfgen` and `xissimarfgen` tools, respectively. Since there are known calibration issues near the Si edge in the XIS detectors near 2 keV (see e.g., Sato et al. 2011; Lohfink et al. 2013), we exclude the 1.7–2.3 keV energy range from all of our spectral fits. Prior to producing the light curves, the event arrival times were corrected to the solar system barycenter using the `barycorr` tool. Since the *Suzaku* XIS time resolution was only 8 s in this observation, we did not use the XIS data for the periodicity search. We also used the (barycentered) *Suzaku* HXD data to investigate the candidate periodic signal reported by Y+20, but we did not use them for spectral

analysis (because of the strong background contamination in this non-imaging instrument). All errors quoted throughout the paper are reported at the 1σ level, unless otherwise noted.

3. TIMING ANALYSIS

A fully coherent periodicity search for an observation with a length comparable to the LS 5039 binary period is a “needle in a haystack” type problem. The large uncertainties in the orbital ephemeris (see Table 1) require a prohibitively large grid in the multidimensional parameter space to guarantee that the periodic signal is not missed (see the discussion in Caliandro et al. 2012). An alternative approach is to segment the observation into multiple time intervals during which the radial velocity of the compact object is approximately constant, and search for periodicity within each segment by analyzing the distribution of Fourier power in the time-frequency domain (a dynamic power spectrum search; e.g., Lorimer & Kramer 2012).

Such an approach was employed by Y+20 (who found a period candidate $P = 9.05$ s in the *NuSTAR* data). These authors only searched for a signal with period $P > 1$ s. They justify this restriction due to the relatively small number of photons in the 10–30 keV band chosen for the periodicity search in the *NuSTAR* data. Furthermore, they justify this energy band selection by the fact that the 8.96 s period candidate was seen in *Suzaku* HXD, which is only sensitive above 10 keV. However, we see no reason for the signal not to be present below 10 keV because there is no change in the source spectrum (see Section 4). Since we cannot exclude the possibility that the true period is different from that claimed by Y+20, we perform a period search in a broader range of frequencies and a different energy range.

To improve the sensitivity by decreasing the spread of the potential signal in the frequency domain, we (1) use an optimal division into time segments that depends on the frequency intervals we are searching in, (2) introduce a statistic that provides a higher sensitivity to a signal than the simplistic incoherent summing of Fourier powers from non-overlapping time intervals within the observation, and (3) apply the Römer delay correction (e.g., Blandford & Teukolsky 1976) to the photon arrival times using the best known ephemeris. Then we perform the dynamic pulsation search. This approach allows us to search up to much higher frequencies (e.g., 1000 Hz) than the 1 Hz limit used in Y+20.

Since the nature of the compact object is unknown, we adopt the approach, described in Section 3.2.3, which allows us to search for both periodic signals and quasi-periodic oscillations (QPOs). We also perform a burst-

³ See <https://heasarc.gsfc.nasa.gov/docs/suzaku/analysis/abc/>.

like variability search (on scales from 1 s to 200 s) and orbital variability characterization on larger timescales (Section 3.4).

3.1. Correction for the Römer delay caused by the orbital motion

As the putative pulsar is orbiting a massive star, the distance between the pulsar and the observer changes with orbital phase, which translates into changing times of photon travel to the observer. This effect can be equivalently described in the observer’s frame as a Doppler shift of the pulsation frequency varying with the binary phase because of the changing radial velocity of the pulsar. Different authors have inferred slightly different sets of orbital parameters from optical observations of the massive companion (see examples in Table 1). To correct the event arrival times for this effect (Römer delay), we adopted the ‘eccentric fit + 1d oscillation’ orbital solution from Casares et al. (2011), which included modulation of the radial velocity with a 1 day period, possibly caused by non-radial oscillations of the massive companion in its eccentric orbit. The orbital dependencies of the Römer delay and Doppler shift of the other published binary solutions are within $\approx \pm 1\sigma$ uncertainties of the Casares et al. (2011) curves for these quantities (see Figure 1 and Figure 10 in the Appendix).

The projection of the orbit’s semi-major axis onto the sky plane, $a \sin i$, and the longitude of periastron, W , in Casares et al. (2011) (and the other papers quoted in Table 1) pertain to the massive stellar component of the binary. They are connected with the corresponding compact object parameters as follows,

$$a_p \sin i = \frac{m_*}{m_p} a_* \sin i, \quad W_p = W_* - 180^\circ, \quad (1)$$

where the subscripts $*$ and p correspond to the massive star and the compact object (putative pulsar), respectively, m is mass, and i is the orbital inclination (the angle between the orbital plane and the plane of the sky). For the pulsar (NS) mass we use $m_p = 1.8_{-0.6}^{+0.2} M_\odot$, from the assumption that m_p should be in the range of 1.2–2.0 solar masses, which gives $a_p \sin i = 52_{-19}^{+9} \text{ lt-s} = (1.55_{-0.6}^{+0.27}) \times 10^{12} \text{ cm}$.

The corrections to the photon arrival times due to orbital motion (Römer delay) are calculated as follows,

$$t_{\text{corr}} = t - \frac{a_p \sin i}{c} \left[\sin W_p (\cos E - e) + \sqrt{1 - e^2} \cos W_p \sin E \right]. \quad (2)$$

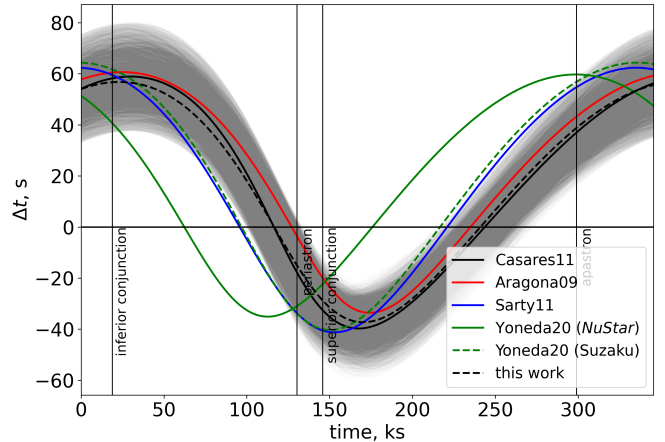


Figure 1. Arrival time corrections due to Römer delay during our *NuSTAR* observation for 6 sets of orbital parameters (see Table 1). Shown is $\Delta t = t_{\text{corr}} - t$ vs. t , given by Equation (2). The shaded area shows the uncertainty of Δt due to the uncertainties of the orbital parameters for the binary ephemeris from Casares et al. (2011) (the model with 1 d oscillations).

Here e is the eccentricity of the orbit, and E is the eccentric anomaly,

$$E - e \sin E = \Omega_{\text{orb}}(t - T_0), \quad (3)$$

where $\Omega_{\text{orb}} = 2\pi/P_{\text{orb}}$, P_{orb} is the orbital period, and T_0 is the epoch of periastron (Blandford & Teukolsky 1976). The right hand side of Equation (3) is commonly called the mean anomaly. Depending on the orbital phase, the correction ranges from -40 s to $+60$ s (see Figure 1).

3.2. Periodicity search in the *NuSTAR* data

We searched for periodic or quasi-periodic signals up to $f_{\text{max}} = 1000$ Hz by analyzing the arrival times of $N = 56\,647$ events, registered during ≈ 190 ks (when the target was not occulted by the Earth), in the photon energy range of 3–20 keV. We excluded higher energies to reduce the background contamination as *NuSTAR*’s sensitivity decreases at higher energies. We corrected the event arrival times for the Römer delay using the best-fit binary parameters from Casares et al. 2011 (Table 1) prior to the search.

3.2.1. Fourier power spectrum for the entire *NuSTAR* observation assuming the binary parameters are known with high precision

Using the corrected arrival times from the entire *NuSTAR* observation, we calculated the Fourier power spectrum (see the top panel of Figure 2 and the Appendix A). The top panel of Figure 2 shows the values of the Fourier power \mathcal{P}_n as a function of frequency $f = n \Delta f$,

Table 1. Orbital parameters for LS 5039 inferred from different observations

	Aragona09	Casares11	Sarty11	Yoneda20	Yoneda20	this work
				NuSTAR	Suzaku	
P_{orb} (d)	3.90608 ± 0.00010	3.90608 ± 0.00008	3.906	3.90608	3.90608	3.9057 ± 0.28
T_0 (MJD)	52825.48 ± 0.05	52477.58 ± 0.06	55016.58 ± 0.06	$57629.250^{+0.023}_{-0.030}$	$54352.455^{+0.05}_{-0.035}$	57633.71 ± 0.06
e	0.337 ± 0.036	0.35 ± 0.03	0.24 ± 0.08	$0.306^{+0.015}_{-0.013}$	$0.278^{+0.014}_{-0.023}$	0.289 ± 0.09
W_* (deg)	236 ± 5.8	212 ± 5	237.3 ± 21.8	$236.8^{+2.3}_{-3.1}$	$234.6^{+5.1}_{-3.3}$	
$a_* \sin i$ (lt-s)	3.33 ± 0.15	4.06 ± 0.16	4.11 ± 0.35			
W_p (deg)	56 ± 5.8	32 ± 5	57.3 ± 21.8	$56.8^{+2.3}_{-3.1}$	$54.6^{+5.1}_{-3.3}$	44.6 ± 4.1
$a_p \sin i$ (lt-s)	48 ± 14	52^{+9}_{-19}	52^{+10}_{-19}	48.1 ± 0.4	$53.05^{+0.7}_{-0.55}$	48.1 ± 2.7

NOTE—Orbital parameters from [Aragona et al. \(2009\)](#), [Casares et al. \(2011\)](#), [Sarty et al. \(2011\)](#), Y+20 and this work. Subscripts $*$ and p correspond to the massive star and the compact object (putative pulsar), respectively. For the [Aragona et al. \(2009\)](#), [Casares et al. \(2011\)](#), and [Sarty et al. \(2011\)](#) orbital solutions, the projected semi-major axis $a_p \sin i$ was calculated assuming $m_* = (23 \pm 3)M_\odot$ while the compact object’s mass was assumed to be $m_p = (1.6 \pm 0.4)M_\odot$ for [Aragona et al. \(2009\)](#) and $m_p = 1.8^{+0.2}_{-0.6}M_\odot$ for [Casares et al. \(2011\)](#) and [Sarty et al. \(2011\)](#). We use the [Casares et al. \(2011\)](#) orbital parameters for the Römer delay correction. The Y+20 and ‘this work’ parameters were not measured from observations of the massive star but obtained from fits maximizing the significance of the putative period near 9.05 s. The large uncertainties of the ‘this work’ parameters take into account the multitude of solutions of about the same significance in the vicinity of the best-fit solution (see Section 3.3).

where $\Delta f \simeq 3 \times 10^{-7}$ Hz is the frequency bin width (only 24,448 power values with $\mathcal{P}_n > 20$ are shown). The power is normalized in such a way that the mean $\overline{\mathcal{P}_n} = 2$ for a Poisson-distributed noise. The high values of \mathcal{P}_n at low frequencies, $f \lesssim 0.003$ Hz, are associated with the periodic motion of the NuSTAR satellite around the Earth (the frequency of NuSTAR revolution, 1.72×10^{-4} Hz, and its 15 harmonics are shown by blue vertical lines). At higher frequencies none of the \mathcal{P}_n values is outstanding, and their significances do not exceed 4σ . Thus, we conclude that no significant periodic signal is detected.

To look for quasi-periodic signals, we increased the width of frequency bins by factors of 10, 100, and 1000 (compared to the natural width $T_{\text{obs}}^{-1} \approx 2.89 \mu\text{Hz}$) but found no outstanding peaks in the binned Fourier power spectra.

3.2.2. Fourier spectra in separate NuSTAR orbits

The apparent lack of pulsations in the Fourier power spectrum of the entire observation could be due to a large difference between the actual binary parameters and the parameters used for the Römer delay correction. Because of this difference, the binary-phase-dependent frequency shift may not be fully compensated by the Römer delay correction. As a result, the signal coherence would be lost, the power peak corresponding to the (unknown) pulsation frequency would be spread over many frequency bins, and the peak’s height would be strongly reduced. To mitigate the coherence loss,

we search for pulsations in much shorter time segments, corresponding to the intervals of visibility of LS 5039 in the 60 consecutive NuSTAR orbits covered by our observation. During the relatively short intervals (3.2 ks on average) the difference between the actual and best-fit radial velocities of the compact companion does not change as much as over the entire orbit, and there is a higher chance that the signal coherence is preserved.

Similar to the search in the entire NuSTAR observation, we calculated 60 Fourier power spectra and corresponding signal detection significances. The results are shown in the bottom panels of Figure 2 as time-frequency images in which the power and detection significance values are shown by the brightness of the image ‘‘pixels’’. The vertical light and dark stripes correspond to intervals of visibility and occultation of LS 5039, respectively.

If pulsations were detected, they would be seen as a sequence of brighter (lighter) pixels along the time axis at frequencies around the pulsation frequency. If the actual binary parameters coincided with the assumed ones, this sequence would be seen as a horizontal stripe parallel to the time axis. Deflections of the brighter pixels from a horizontal stripe would provide the difference between the actual values of the radial velocity and the ones used in the Römer delay correction, in separate NuSTAR orbits.

We see from the bottom-right panel of Figure 2 that the search in separate NuSTAR orbits also did not pro-

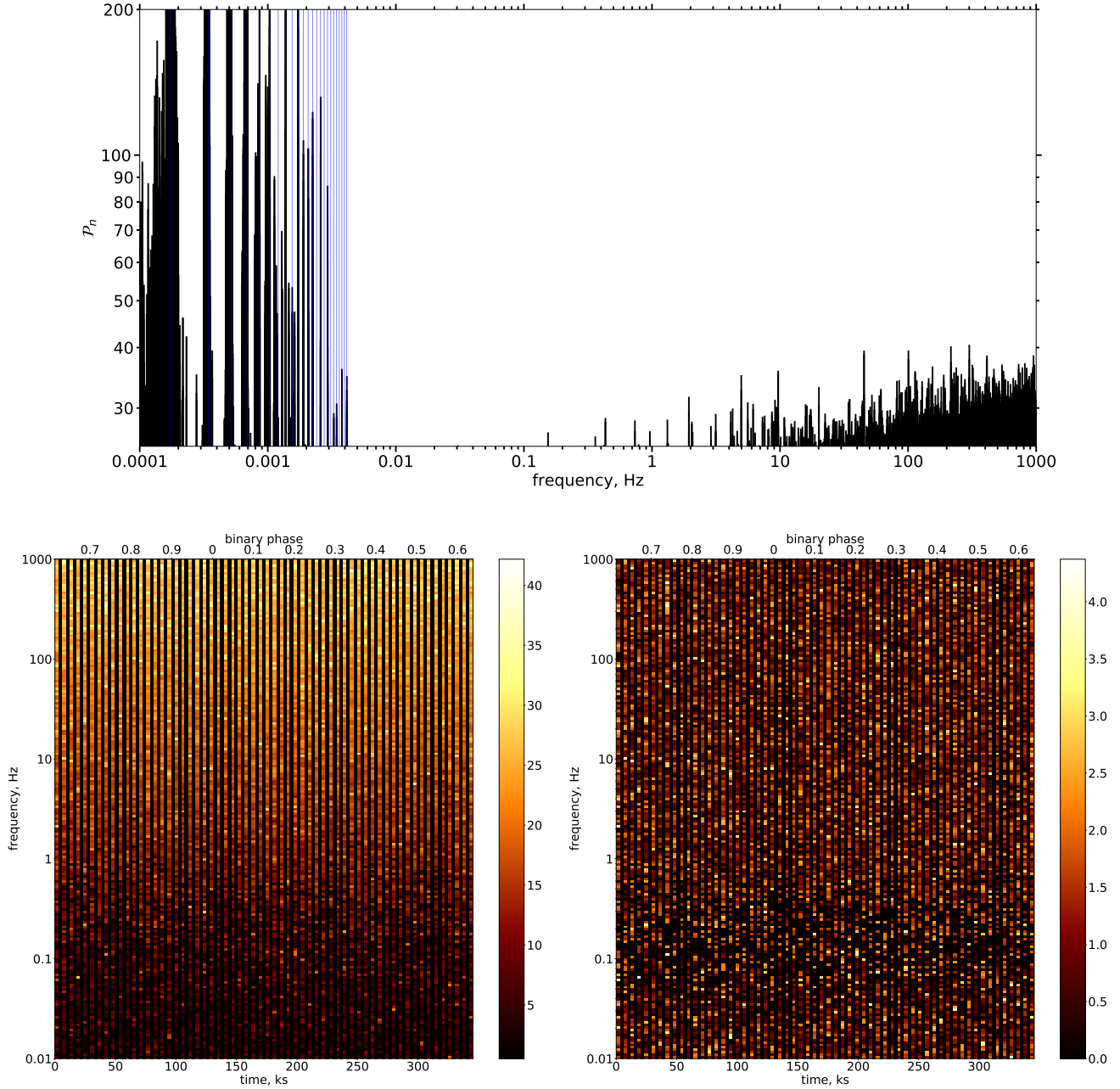


Figure 2. The top panel shows the Fourier power spectrum \mathcal{P}_n , calculated from the entire *NuSTAR* observation (see Appendix A and Section 3.2.1). Prior to calculating the Fourier power spectrum, the arrival times of photons (with energies restricted to the 3–20 keV band) were corrected for the Römer delay using the best-fit orbital parameters from Casares et al. (2011) (see Table 1). The vertical blue lines correspond to the *NuSTAR* orbital period and its harmonics. The bottom panels show the dynamic (time-resolved) spectra of Fourier power and significance, calculated individually for each of the 60 *NuSTAR* orbits, after applying the same Römer delay correction (see Section 3.2.2 and Appendix A). To improve the visualization quality, we do not show power (and significance) values in each frequency bin but instead divide the entire log-frequency range in 200 segments of equal size and plot (using color) the maximum Fourier power, \mathcal{P}_k^{\max} (left), within the k -th segment and its significance, α_k (right). The vertical black stripes are the gaps due to the occultation of LS 5039 by the Earth.

vide periodicity detection. Although some of the α_k values may appear marginally significant, one has to keep in mind that α_k is defined for a single *NuSTAR* orbit (see the Appendix A), and the true significance is therefore lower when all orbits are included (due to the larger number of statistical trials). Moreover, we do not see any extended (along the horizontal direction) connected clusters of adjacent pixels.

The lack of detection could be due to the lower sensitivity of this search. The first reason for the sensitivity loss is the smaller number of counts in separate orbits than in the entire observation (on average, 994 versus 56,647 counts). Since, for a periodic signal with a given pulsed fraction, the power \mathcal{P}_n is proportional to the number of counts, weak pulsations would not be detected.

The second reason for the sensitivity loss is the spread of signal frequency over several frequency bins caused by the Doppler shift. In the i -th *NuSTAR* orbit, the spread associated with the Doppler shift unaccounted for by the Römer delay correction can be estimated as $(\delta f)_i \sim f |\Delta \dot{v}_{\parallel,i}| T_i / c$, where T_i is the visibility interval, and $\Delta \dot{v}_{\parallel,i}$ is the difference between the assumed and actual radial accelerations of the binary motion in the middle of the i -th orbit (see Appendix B). This spread becomes greater than the natural width T_i^{-1} of the frequency bin for $f > \tilde{f}_i \sim c (|\Delta \dot{v}_{\parallel,i}| T_i^2)^{-1} = 3.9 [|\Delta \dot{v}_{\parallel,i}| / (3 \text{ m s}^{-2})]^{-1} [T_i / (3.15 \text{ ks})]^{-2}$ Hz. At a frequency f substantially higher than \tilde{f}_i the peak in the signal power is spread over f/\tilde{f}_i bins, and the peak height will be reduced by about the same amount.

3.2.3. Search for pulsations in a dynamic Fourier spectrum with frequency-dependent time windows

Since the Römer delay correction is imperfect due to the binary ephemeris uncertainties, a periodic signal with a certain frequency f_0 in the reference frame of the pulsar can be spread by the Doppler effect over a number of neighboring frequency bins in the observer's reference frame (see the Appendix B for details). This spread can be mitigated by splitting the observation duration T_{obs} into N_w shorter time windows of a length $T_w = T_{\text{obs}}/N_w$ (hence wider frequency bins T_w^{-1}), but then the signal can be shifted to different frequencies f in different time windows. In order to maximize the sensitivity to such a signal, one should select optimal lengths of the time windows and use an efficient algorithm for detecting the signal in the time-frequency domain.

The optimal lengths of the time windows are determined by the requirement that the maximum possible drift in frequency does not exceed T_w^{-1} . Such choice of T_w is optimal because if one chooses an even smaller T_w ,

then events are lost (as the number of events is proportional to T_w) and the Fourier power decreases.

As we show in Appendix B, the optimal lengths and numbers of time windows depend on the signal frequency ($T_w \sim 9.9 f_0^{-1/2}$ ks, $N_w \sim 35 f_0^{1/2}$ in our case). For practical purposes, it is convenient to divide the entire 0–1000 Hz frequency range into 7 broad frequency intervals with different numbers and lengths of time windows. For each of these time windows we calculate the Fourier power spectrum \mathcal{P}_n in the 0–1000 Hz frequency range, with a frequency resolution of T_w^{-1} .

As the next step, we split the entire frequency range into segments $f_m(1-\beta) < f < f_m(1+\beta)$, where the coefficient β is proportional to $\delta v_{\parallel}/c$, δv_{\parallel} is the maximum residual uncertainty of the pulsar's radial velocity in the appropriate time window, and the central frequency f_m of the m -th segment ($m = 1, 2, \dots$) satisfies Equation (B13). The segment width $2\beta f_m$ must be large enough to ensure that the entire signal, whose Doppler-shifted frequency f is varying with time, is contained within this segment (see Figure 12 in the Appendix).

Each of these segments (their total number is about 2880, for the chosen $\beta = 0.0022$ in the 0.01–1000 Hz range) is inspected for the presence of signal signatures. Any chosen segment is within one of the seven broad frequency intervals, described in the Appendix B, which determines the number N_w and length T_w of the time windows (hence the choice of the precalculated Fourier power spectra) appropriate for the segment analysis.

In the time-frequency plane, an m -th frequency segment consists of N_w time windows and $N_f = 2\beta f_m T_w$ frequency bins, i.e., of $N_w \times N_f = 2\beta f_m T_{\text{obs}} = 690(\beta/10^{-3})f_m$ elements for which Fourier powers $\mathcal{P}_{n,j}$ have been calculated (n and j number the frequency bins and time windows, respectively). To locate possible signal signatures in the segment, we pinpoint the largest values $\mathcal{P}_j^{\text{max}}$ in the sets of N_f powers $\mathcal{P}_{n,j}$ within each of the time windows j . If the $\mathcal{P}_j^{\text{max}}$ values represent a sufficiently strong signal, then the mean of these values over the entire time of observation

$$\mu = \frac{1}{N_w} \sum_{j=1}^{N_w} \mathcal{P}_j^{\text{max}}, \quad (4)$$

should significantly exceed a similarly defined mean for the noise, μ_{noise} .

To characterize the significance of a possible excess of the measured μ over μ_{noise} , we introduce the following s -statistic:

$$s = (\mu - \mu_{\text{noise}}) / \sigma_{\text{noise}}, \quad (5)$$

which provides the signal significance in units of standard deviation. Here, σ_{noise} is the standard deviation of the noise.

Because the observed data contain numerous time gaps, and the count rate changes with time, we used Monte-Carlo simulations to infer μ_{noise} and σ_{noise} for each N_w (when simulating noise, we included gaps larger than 60 s).

In the right panel of Figure 3 we plot the s -statistic values for each of 1261 frequency segments in which s is positive (the total number of frequency segments is 2496 in the 0.017–1000 Hz range). Although there are several peaks slightly exceeding the 3σ level (i.e., $s > 3$), no signal candidates are passing the 4σ threshold.

This panel also shows the s -statistic values computed for six simulated periodic sinusoidal test signals with varying levels of signal strength (characterized by the signal fraction p , with $1-p$ being the unpulsed fraction) that are imperfectly corrected for the Römer delay (see the time-frequency images in Figure 12 in Appendix B). We see that the detectability of a signal with a given signal fraction strongly depends on the signal’s frequency (the higher the frequency the larger p must be for the signal to be detected). At plausible young pulsar frequencies ~ 3 –100 Hz, the signal fractions should significantly exceed 0.1–0.2 to be detected with this method in the available *NuSTAR* data.

For the low-frequency part of the Fourier power spectrum, (Figure 3, left panel) we use the more conventional H -statistic, defined as $H = \max\{Z_m^2 - 4m + 4\}$ for $1 \leq m \leq 20$ (de Jager et al. 1989), where Z_m^2 is the statistic commonly used in periodicity searches in X-ray and γ -ray astronomy (see, e.g., Buccheri et al. 1983). This is possible because for $f \lesssim 0.01$ Hz the residual drift due to the imperfect Römer delay correction does not exceed the natural width ($\sim T_w^{-1}$) of the peak in H -statistic spectrum during the entire observation (i.e., $N_w = 1$; see the Appendix B). Although the H -statistic values at lower frequencies are high, they mostly coincide with multiple integers of the *NuSTAR* orbital frequency (shown by blue vertical lines) while the others are likely to be aliases due the visibility gaps that are somewhat varying in their duration. No credible signal is detected.

3.3. $P = 9.05$ s candidate

Y+20 searched the *Suzaku* HXD data of 2007 September for periodic signals with periods $P > 1$ s in the 10–30 keV band. They found maximum $Z_4^2 = 68.0$ (the other Z_n^2 values were not reported) at $f_{\text{HXD}} = 0.1116510(5)$ Hz, or $P_{\text{HXD}} = 8.95648(4)$ s, with the estimated significance of 98.8%.

In a subsequent search in the above-described *NuSTAR* data (191 ks net observing time, 12,000 events in the 10–30 keV energy band, and assuming $P >$

1 s) Y+20 obtained a maximum $Z_4^2 = 66.9$ at $f_{\text{NuST}} = 0.1104507(4)$ Hz or $P_{\text{NuST}} = 9.05381(3)$ s, with an estimated significance of only 93%.

To find these period values, Y+20 varied the orbital parameters in the ranges provided in Table 1 of that work, applied the Römer delay correction for each parameter set, and chose the set, and the corresponding period, that maximized the Z_4^2 value. The uncertainties of the periods given in Y+20 appear to be underestimated because they do not account for the uncertainties in the ephemeris parameters (as we show below). Y+20 concluded that two incompatible sets of orbital parameters are needed to maximize the strength of the *NuSTAR* and *Suzaku* candidate periodic signals. Moreover, the ephemeris that maximizes the periodic candidate signal in the *NuSTAR* data is incompatible with any previously published ephemeris (within their uncertainties; see Table 1 and Figure 1).

To verify the period and the significance reported by Y+20, we have performed an independent period search in the *NuSTAR* data around $P = 9.05$ s. Choosing a set of 5 orbital parameters within the 2σ uncertainties of the Casares et al. (2011) ephemeris, we applied the Römer delay correction to the times of arrival, calculated $Z_m^2(f)$ for $m = 1, \dots, 20$ (using events from the entire observation) in the frequency interval of (0.109–0.113) Hz, and used the H -test (de Jager et al. 1989) to determine the maximum number of significant harmonics. Varying the orbital parameters on the 5-dimensional grid, we found the parameter set that maximizes Z_m^2 and the corresponding frequency. We repeated these calculations for various energy ranges within 3–40 keV and various source aperture radii up to $r = 60''$ to choose an optimal (maximizing Z_m^2) energy range and aperture radius. As a result, in the 10–18 keV energy range and for the aperture radius $r = 38''$, we found a signal (shown in Figure 5) with maximum $Z_1^2 = 60$ at $f = 0.1104977$ Hz ($P = 9.049962$ s). In the $Z_m^2(f)$ dependence, the peak at $f = 0.1104977$ Hz is surrounded by many other peaks with slightly lower heights, including a peak at $f = 0.1104507$ Hz reported by Y+20. These peaks, appearing at different combinations of orbital parameters, look virtually as significant as the highest one, so that we cannot prefer one peak to another. Therefore, the true uncertainty of the putative pulsation frequency (and the fitted orbital parameters) is determined not by the width of a separate peak but by the width of the entire ‘cluster of peaks’, $\sim 3 \times 10^{-5}$ Hz in our case, which is about two orders of magnitude larger than the uncertainty claimed by Y+20. Accounting for this uncertainty, the frequency and period of the putative pulsations are $f = 0.11050(3)$

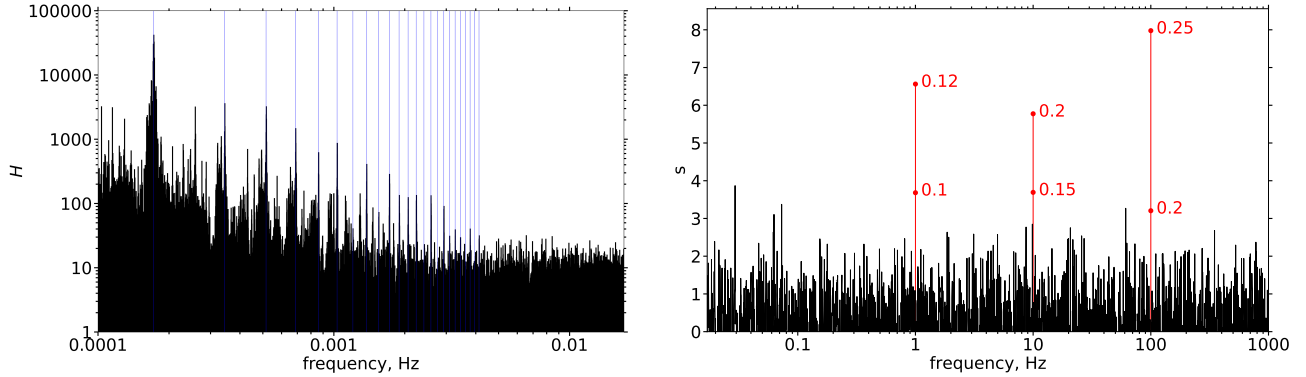


Figure 3. Left panel shows the H statistic calculated for the frequencies up to 0.017 Hz. Blue vertical lines correspond to the orbital frequency of *NuSTAR* (1.7×10^{-4} Hz) and its harmonics. The H -statistic peaks are aliases caused by the presence of quasi-periodic gaps (the gap width varies slightly with time) due to the occultation of the target by Earth during the long *NuSTAR* observation and SAA passages. Right panel shows all positive s -statistic values (see Equation 5) in 1261 frequency segments between 0.017 Hz and 1000 Hz. Dots on red vertical lines show the s values for the (artificial) test signals (see the description and Figure (12) in the Appendix B); the numbers near the dots are the signal fractions.

Hz and $P = 9.050(2)$ s), for the orbital parameters listed in the column ‘this work’ of Table 1.

We note that higher harmonics are not required by the H -test. However, for comparison with Y+20, who reports Z_4^2 , we also calculated it and found $Z_4^2 = 71$ for our best fit, at $f = 0.1104977$ Hz. We also note that our optimal orbital parameters are much closer to those found in the previous papers than the set of parameters suggested by Y+20 (see Figures 1 and 10).

To explore the distribution of the Fourier power as a function of time (or binary phase), we calculated a time-resolved Fourier spectrum, i.e. the Z_1^2 distribution in the time-frequency plane around $f = 0.110498$ Hz ($P = 9.04996$ s). To reduce the effect of time gaps, we used a sliding time window with the size of $T_{\text{obs}}/10$ which is moved by 10% at each step (see Figure 4). The plots show that the strongest contribution to the signal comes from a time interval close to the end of the *NuSTAR* observation (between 270 and 330 ks, counted from the start of the observation), near the binary apastron.

We note that the s -statistic, introduced in Section 3.2.3, is not sensitive to such a signal because the Fourier power does not remain constant during the observation time span. Figure 5 shows the Z_1^2 distribution calculated from the entire observation around $f = 0.110498$ Hz ($P = 9.04996$ s) and the corresponding folded pulse profiles from the entire observation and from the part of it with the strongest signal.

In addition, we re-analyzed the *Suzaku* HXD data and confirmed the signal candidate reported by Y+20, with maximum $Z_4^2 = 67.8$ at $P = 8.95648$ s. We also analyzed jointly the *NuSTAR* and *Suzaku* HXD data, requiring a common binary ephemeris. However, the strongest signal that we were able to find in this case was rather

insignificant, with $Z_1^2 \approx 50$ (Z_m^2 with $m > 1$ were even less significant).

It should also be noted that, among other factors (such as the energy range, aperture, and ephemeris choices), the significance of the 9.05 s periodic signal candidate depends on the maximum frequency of the frequency range searched. There is no physical a priori reason to limit the search to $f < 1$ Hz. Extending the frequency range to much higher frequencies and accounting for the huge number of trials associated with varying the ephemeris parameters, energy range, and extraction aperture would render the putative 9.05 s signal candidate insignificant.

3.4. The binary light curves and search for nonperiodic variability

The background-subtracted light curves of LS 5039 for 3 energy bands are shown in Figure 6 as functions of the binary phase $\phi = \text{frac}[(t - T_0)/P_{\text{orb}}]$, where $\text{frac}[X]$ is fractional part of X , and T_0 and P_{orb} are the best-fit values of the epoch of periastron and binary period taken from Aragona et al. (2009). The light curves grow from minima at $\phi \approx 0.1$ (near superior conjunction, $\phi_{\text{supc}} = 0.046$) up to $\phi \approx 0.4$, then remain nearly flat, with short fluctuations, around apastron ($\phi = 0.5$), show narrow peaks at $\phi = 0.6$ (before inferior conjunction; $\phi_{\text{infc}} = 0.67$), and secondary peaks at $\phi \approx 0.8$. Thus, the light curves exhibit a flat-top maximum, encompassing the apastron and inferior conjunction phases. If, instead of the ephemeris from Aragona et al. (2009), we use the ephemeris from Casares et al. (2011) or Sarty et al. (2011) for folding and/or calculating the conjunction phases, the shifts will not exceed 0.1 in phase.

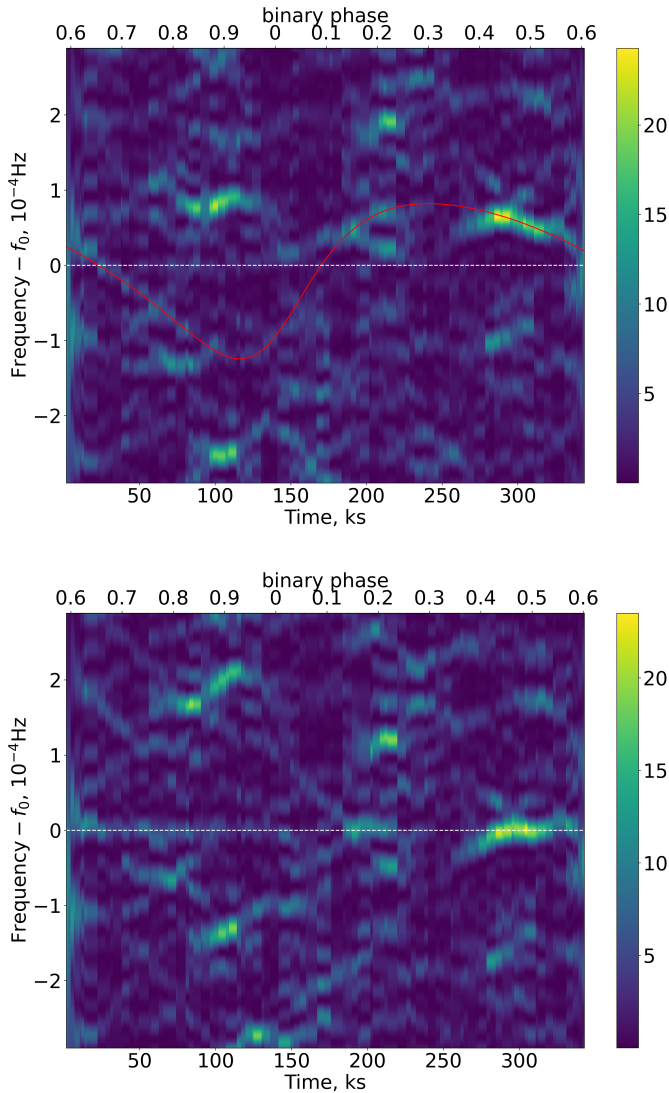


Figure 4. The top panel shows Z_1^2 as a function of frequency and time near $f_0 = 0.110498$ Hz ($P_0 = 9.04996$ s), shown by the dashed horizontal line. The Z_1^2 was calculated using events extracted from the $r = 38''$ aperture in the 10–18 keV band. The red curve shows the Doppler shift due to the orbital motion as a function of the observation time for the orbital parameters that we found (see Table 1). The bottom panel shows the same thing as the top panel but the photon arrival times are corrected for the orbital motion with this ephemeris. In both cases the color bars show the value of Z_1^2 per time window.

The overall structure of the light curves does not evolve noticeably with energy, not only within the *NuSTAR* band but also between the *Suzaku* XIS and *NuSTAR* bands (see Takahashi et al. 2009). It also does not show appreciable changes between the *Suzaku* XIS and *NuSTAR* observations, separated by 9 years.

We have also searched the data for short aperiodic variability, such as bursts. We binned the arrival times to produce light curves with bin sizes varying from 1 to 200 s (so that the largest bins are smaller than the smallest gap in the *NuSTAR* observation). We calculated the Poisson probability, q , of having a number of counts per bin larger than measured. Note that the average number of counts per bin (the Poisson distribution parameter) varies with the binary phase. This is taken into account by calculating a local mean over ≈ 3000 s time interval (slightly larger than the largest gap in the *NuSTAR* observation) surrounding the bin for which the probability is calculated (this bin itself is excluded from the mean calculation). For the chosen bin size, the Poisson probability should be corrected for the number of trials, N_{tr} , which is equal to the number of bins, N_{bin} , in the entire *NuSTAR* observation: $q_{\text{corr}} = 1 - (1 - q)^{N_{\text{bin}}}$. Figure 7 shows two most significant bursts that we found. The burst durations are about ~ 1 s and ~ 70 s. With the above definition of probability, the significances are 3.6σ for the short burst and 3.2σ for the longer burst. However, we note that this probably was derived for a fixed number of bins. If we account for all possible binning schemes (not just the one that results in the highest significance), then $N_{\text{tr}} > N_{\text{bin}}$, i.e., the confidence levels become lower. Therefore, these two burst candidates are not truly significant.

4. SPECTRAL ANALYSIS

4.1. Phase-integrated spectroscopy

We analyzed the *NuSTAR* and *Suzaku* spectra using XSPEC ver. 12.9.1p (Arnaud 1996). To account for interstellar absorption, we used the Tübingen-Boulder model (`tbabs` in XSPEC) with the photo-electric cross-sections of Verner et al. (1996) and the abundances of Wilms et al. (2000). We bin the spectra to have $S/N \simeq 7$ in each spectral bin, corresponding to 50 counts per bin, and used the χ^2 statistic for model parameter estimation and error calculation. For all spectral fits, we added multiplicative constants to the FPMA and FPMB normalizations, frozen to 1 for the former and allowed to vary for the latter, to account for calibration uncertainties between the two detector modules. We found the difference in the normalization factors not exceeding 2%. We also found, using the same approach, that the calibration uncertainty between the *NuSTAR* and *Suzaku* instruments is around 10%.

LS 5039 is detected with *NuSTAR* up to 70 keV, with a background-corrected count rate of $0.186(1)$ cts s^{-1} and $0.171(1)$ cts s^{-1} , in the FPMA and FPMB detectors, respectively, in the 3–70 keV energy range, with a background contribution of $< 10\%$ in each detector.

The number of background-corrected counts in the 60–70 keV energy range is about 45 ± 12 in each module with a background contribution of ≈ 70 –80%, i.e., the source becomes hardly distinguishable from the background at higher energies. An absorbed PL model gives a statistically acceptable fit to the phase-integrated spectrum in the 3–70 keV band, with $\chi^2 = 667$ for 708 degrees of freedom (dof). We find a hydrogen column density $N_{\text{H}} = (0.7 \pm 0.4) \times 10^{22} \text{ cm}^{-2}$, a photon index $\Gamma = 1.61 \pm 0.01$, and an absorption-corrected energy flux $F_{3-70 \text{ keV}} = (2.31 \pm 0.02) \times 10^{-11} \text{ erg s}^{-1} \text{ cm}^{-2}$. There are no indications of spectral features in the fit residuals, including around the Fe K α line complex at 6–7 keV. Moreover, considering the *NuSTAR* spectra alone, we find no evidence of a high-energy cutoff usually present in the hard X-ray spectra of HMXBs harboring accreting neutron stars (see, e.g., Coburn et al. 2002; Krivonos et al. 2015; Fornasini et al. 2017). The photon index as inferred from the *NuSTAR* spectra is larger than $\Gamma = 1.51 \pm 0.01$ found at lower X-ray energies with *Suzaku* (Takahashi et al. 2009).

Given the long-term stability of the binary’s periodic X-ray light curve, (Kishishita et al. 2009), we fit the *NuSTAR* 3–70 keV and the *Suzaku* 0.7–10 keV phase-averaged spectra simultaneously with an absorbed PL model (Figure 8). We linked all parameters among the two spectra, except for a constant normalization to take into account calibration uncertainties between the instruments. We find a statistically acceptable fit to the data ($\chi^2 = 2722$ for 2795 dof), with $N_{\text{H}} = (1.18 \pm 0.01) \times 10^{22} \text{ cm}^{-2}$, $\Gamma = 1.588 \pm 0.007$ (Table 2), and absorption-corrected fluxes $F_{0.5-10 \text{ keV}} = (9.64 \pm 0.05) \times 10^{-12} \text{ erg s}^{-1} \text{ cm}^{-2}$, and $F_{10-70 \text{ keV}} = (18.0 \pm 0.2) \times 10^{-12} \text{ erg s}^{-1} \text{ cm}^{-2}$. These fluxes correspond to a luminosity $L_{0.5-70 \text{ keV}} \approx 2.8 \times 10^{34} (d/2.9 \text{ kpc})^2 \text{ erg s}^{-1}$.

4.2. Phase-resolved spectroscopy

We performed broad-band phase-resolved spectroscopy using the *Suzaku* XIS and *NuSTAR* data to look for modulation of spectral parameters with the orbital period. We used the same definition of binary phase as for the light curve shown in Figure 6. We extract the spectra in orbital phase bins $\Delta\phi = 0.1$ ($\phi = 0$ corresponds to binary periastron). Because of lower count statistics in the chosen phase bins, we bin the spectra to 5 counts per energy bin and use the Cash statistic. We fit all 10 spectra simultaneously with an absorbed PL. Given that phase-resolved spectroscopy with *Suzaku* alone revealed no variability in the hydrogen column density (Takahashi et al. 2009), we linked N_{H} between all spectra, but left the photon index and

Table 2. Spectral parameters of LS 5039 from joint PL fits to the *NuSTAR* and *Suzaku* data

Phases	N_{H} 10^{22} cm^{-2}	Γ	Flux (3-70 keV) $10^{-11} \text{ erg s}^{-1} \text{ cm}^{-2}$
0.0 – 1.0	1.18 ± 0.01	1.588 ± 0.007	2.31 ± 0.02
0.0 – 0.1	0.5 ± 0.4	1.67 ± 0.02	1.24 ± 0.03
0.1 – 0.2	...	1.65 ± 0.02	0.98 ± 0.03
0.2 – 0.3	...	1.62 ± 0.02	1.63 ± 0.04
0.3 – 0.4	...	1.57 ± 0.02	2.56 ± 0.06
0.4 – 0.5	...	1.56 ± 0.01	3.12 ± 0.06
0.5 – 0.6	...	1.57 ± 0.02	3.30 ± 0.05
0.6 – 0.7	...	1.56 ± 0.01	3.48 ± 0.06
0.7 – 0.8	...	1.57 ± 0.02	3.05 ± 0.07
0.8 – 0.9	...	1.59 ± 0.02	2.33 ± 0.05
0.9 – 1.0	...	1.62 ± 0.02	1.45 ± 0.04

the normalization of the PL free to vary. We find a good fit to the spectra with a C-stat of 8950 for 9000 dof.

The fit results are presented in Table 2. Figure 9 shows the flux and photon index variations with orbital phase. We find a strong modulation of the photon index Γ , as similar to those inferred previously from *RXTE* and *Suzaku* observations (Bosch-Ramon et al. 2005; Takahashi et al. 2009). Our *NuSTAR* plus *Suzaku* fits have shown harder spectra than *RXTE* at all phases. The addition of the *NuSTAR* data to the *Suzaku* data has provided tighter constraints on the photon index, showing that it varies by $\Delta\Gamma \approx 0.1$ from maximum to minimum.

A similar tendency was noticed previously in the *RXTE* phase-resolved spectra (3–30 keV band), but the values of Γ and $\Delta\Gamma$ were substantially larger (see Figure 4 in Bosch-Ramon et al. 2005). A similar Γ - F anticorrelation in the 1–10 keV range (*XMM-Newton*, *Chandra*, *ASCA* and *Suzaku* data) is shown by Figure 1 in Kishishita et al. (2009).

5. DISCUSSION AND SUMMARY

The nature of the compact object in LS 5039 has long been elusive. The two main scenarios that are often used for the interpretation of its observed properties are the *microquasar scenario* (radiatively-inefficient accretion onto a BH with the nonthermal emission coming from the jets; e.g., Bosch-Ramon et al. 2005), and the *colliding winds scenario* (the relativistic wind from a young rotation-powered pulsar collides with the massive star’s wind resulting in an intrabinary shock and particle acceleration (Dubus 2006, 2015; Molina & Bosch-

Ramon 2020). In addition, one could also consider the ‘*propeller scenario*’ in which the interaction of the massive star’s wind with the rotating magnetosphere of a strongly magnetized NS can accelerate wind particles to relativistic energies via shocks or magnetic field reconnection. Such a scenario was suggested by Torres et al. (2012) for another HMGB, LSI+61° 303, from which a magnetar-like burst was likely observed, and it was also mentioned by Y+20 as a possibility for LS 5039 if the proposed magnetar nature of the compact object is confirmed. The possibility of accretion onto the NS surface (magnetic poles) seems to be excluded due to the long-term stability of the orbital light curve in X-rays, featureless PL spectrum from 0.3 to ~ 100 keV, low X-ray luminosity, $L_X \approx 2.8 \times 10^{34} (d/2.9 \text{ kpc})^2 \text{ erg s}^{-1}$, and a lack of outbursts.

The detection of fast pulsations, typical for a young rotation-powered pulsar, would strongly support the colliding wind scenario while detection of slow pulsations (e.g., with a few seconds period) could support the scenario with a magnetar propeller, as suggested by Y+20. However, our timing analysis did not yield any evidence for a young pulsar. Although we were able to confirm the Fourier power excess near $P = 9.05$ s, previously reported by Y+20, and find a binary ephemeris compatible with the optical observations (contrary to Y+20), the significance of this excess is rather low. The excess near $P = 8.96$ s found by Y+20 in the *Suzaku* HXD data obtained 9 years earlier could strengthen the magnetar hypothesis, if a large enough \dot{P} is assumed. However, we failed to find a common binary ephemeris which would provide even marginally acceptable signal detections at both 9.05 s (in *NuSTAR*) and 8.96 s (in *Suzaku*). Another *NuSTAR* observation is needed to decisively confirm or rule out the 9 s period candidate and magnetar scenario or, if this period is not confirmed, to perform a more sensitive search for pulsations at other frequencies.

Our variability analysis does not support the accretion scenario. The binary light curve appears to be rather stable over timescales of at least 9 years (between the *Suzaku* and *NuSTAR* observations), including even the fine structure (e.g. the narrow spike near the apastron and inferior conjunction). The stable fine structure cannot be explained by a clumpy stellar wind or instabilities in the accretion flow. Understanding the nature of this stable small-scale structure in the light curve may hold the key to the interaction scenario.

We also looked for bursts on even shorter time scales (< 200 s), which could be expected in the accretion and magnetar scenarios, but found no significant bursting activity. The binary light curve also shows little-to-no dependence on energy in the 0.7–70 keV range. Having

the light curve maximum around the apastron (which is close to the inferior conjunction in LS 5039) phase is hardly compatible with wind accretion (unless the wind has very unusual properties).

The spectral analysis shows that both the phase-integrated and phase-resolved spectra in the 0.7–70 keV range can be fitted by a simple PL model modified by the interstellar extinction. We do not find any evidence of a cutoff at higher energies. The photon index values ($\Gamma \simeq 1.6$ in the phase-integrated spectrum, $1.56 \lesssim \Gamma \lesssim 1.67$ in separate phase bins) are typical for such synchrotron sources as pulsars and PWNe (Kargaltsev & Pavlov 2008). The value of Γ is also typical for other HMGBs (see e.g., Figure 1 from Kargaltsev et al. 2014) but the spread of Γ with the orbital phase is smaller for LS 5039 than those for the other HMGBs, perhaps due to the LS 5039’s tighter orbit.

We have confirmed a statistically significant anti-correlation between the flux and the photon index observed throughout the binary orbit, previously reported by Bosch-Ramon et al. (2005), Takahashi et al. (2009), and Kishishita et al. (2009). This phenomenon may hold another important clue to the nature of the compact object and emission processes in LS 5039 and the other HMGBs. A similar anti-correlation has been seen in at least two other HMGBs: 1FGL J1018.6–5856 (An et al. 2013) and LSI+61°303 (Massi et al. 2017). In the colliding wind scenario, the anti-correlation could be explained by a model in which the observer sees a harder spectrum of emitted electrons at the phases when the flux is increased by, e.g., the Doppler boosting. We see from Figures 9 (and 6) that the flux is maximal and the photon index minimal near inferior conjunction, when the compact object is between the observer and the massive star. This suggests that the Doppler boosting occurs in a shocked pulsar wind confined by the dynamically dominant stellar wind in a (hollow) cone (a paraboloid-like shell) around the star-pulsar direction (see, e.g., left panel in Figures 10 in Dubus 2013). This assumption is supported by simulations by Bogovalov et al. (2012) and Bogovalov et al. (2019) who show that the bulk flow of the shocked pulsar wind can reach a bulk Lorentz factor of a few as the wind is streaming away from the cone apex. In order to explain the anti-correlation between the flux and photon index, one has to assume that particle acceleration in the shocked pulsar wind proceeds more efficiently as the bulk flow accelerates, despite the adiabatic and cooling losses. The mechanism of particle acceleration is unclear but it might be akin to that in extended AGN jets (e.g., the shear acceleration in an expanding flow; Rieger & Duffy 2016).

The hollow cone configuration of the shocked pulsar wind would naturally give rise to a double peaked structure in the light curve (e.g., the peaks at phases 0.4 and 0.8 in Figure 6), as cone crosses the observers line of sight. This would also naturally explain the relatively flat top in the light curve. However in this scenario it is unclear what could cause the third (and strongest) peak, near phase 0.6.

Overall, we conclude that the colliding wind scenario with the compact object being a young pulsar remains the most plausible option as it can explain the dependence of the flux on the binary phase (by Doppler beaming), the spectrum (by synchrotron emission from particles accelerated by the colliding winds), the longer term stability of the light curve, and the lack of variability on short timescales.

Facilities:

Facility: NuSTAR ,

Facility: Suzaku (XRT)

1 Support for this work was provided by the Na-
2 tional Aeronautics and Space Administration through
3 the NuSTAR award NNX17AB77G. JH would like to
4 thank John Tomsick for helpful discussions regarding
5 the reduction of Suzaku data. JH acknowledges sup-
6 port from an appointment to the NASA Postdoctoral
7 Program at the Goddard Space Flight Center, admin-
8 istered by the Universities Space Research Association
9 under contract with NASA. GY acknowledges support
10 from NASA through Fermi grant 80NSSC20K1571.

APPENDIX

A. FOURIER POWER SPECTRA AND PERIODIC SIGNAL SIGNIFICANCE

To compute the Fourier power spectrum for the entire NuSTAR observation ($T_{\text{obs}} = 345,498$ s) up to $f_{\text{max}} = 1000$ Hz using the Fast Fourier Transform (FFT), we first binned the data into $T_{\text{obs}}/\Delta t \approx 6.91 \times 10^8$ time bins with a bin width $\Delta t = (2f_{\text{max}})^{-1} = 0.0005$ s. In order to improve the native frequency resolution ($\Delta f = T_{\text{obs}}^{-1} \approx 2.89 \times 10^{-6}$ Hz) by approximately a factor of 5 (limited by the available computer memory size), we artificially extended the observation time span by that factor and assigned the average value from the real time bins to the added time bins (so that in the resulting Fourier spectrum only the DC component is affected; Ransom, et al. 2002). As a result, we obtained $N_{\text{bin}} \approx 3.46 \times 10^9$. This corresponds to a frequency resolution $\Delta f \approx 3 \times 10^{-7}$ Hz.

The discrete Fourier power spectrum is given by the following equations,

$$\mathcal{P}_n = |s_n|^2, \quad s_n = \sqrt{\frac{2}{N}} \sum_{k=0}^{N_{\text{bin}}-1} a_k \exp\left(-\frac{2\pi i k n}{N_{\text{bin}}}\right), \quad (\text{A1})$$

where n is the frequency bin number, a_k is the number of counts in the k -th time bin, and $N = 56,647$ is the total number of counts (in the 3–20 keV energy range). The corresponding Fourier power spectrum (for times of arrival corrected for the Römer delay with the best-fit orbital parameter of LS 5039) is shown in the upper left panel of Figure 2, where we only plot 24,448 power values exceeding $\mathcal{P}_n = 20$.

For Poisson noise, the power in n -th frequency bin is distributed according to the exponential distribution

$$\varphi(\mathcal{P}_n) = \frac{1}{2} \exp\left(-\frac{\mathcal{P}_n}{2}\right), \quad (\text{A2})$$

with the mean value $\bar{\mathcal{P}}_n = 2$ (i.e., the same mean as for the often-used Z_1^2 statistic; Buccheri et al. 1983). The probability of obtaining, in the Poisson noise, at least one value of power greater than \mathcal{P}_n in $N_{\text{tr}} = T_{\text{obs}}f_{\text{max}}$ independent trials is

$$\Pr(\mathcal{P} > \mathcal{P}_n) = 1 - \mathcal{S}_n, \quad \mathcal{S}_n = \left[\int_0^{\mathcal{P}_n} \varphi(x) dx \right]^{N_{\text{tr}}} = \left[1 - \exp\left(-\frac{\mathcal{P}_n}{2}\right) \right]^{N_{\text{tr}}} \quad (\text{A3})$$

The value of \mathcal{S}_n determines the likelihood of the hypothesis that the power \mathcal{P}_n is generated by a periodic signal with frequency $n \Delta f$ rather than by the Poisson noise.

Following tradition, we chose to characterize the n -th power value by the parameter

$$\alpha_n = \sqrt{2} \operatorname{erf}^{-1} \mathcal{S}_n, \quad (\text{A4})$$

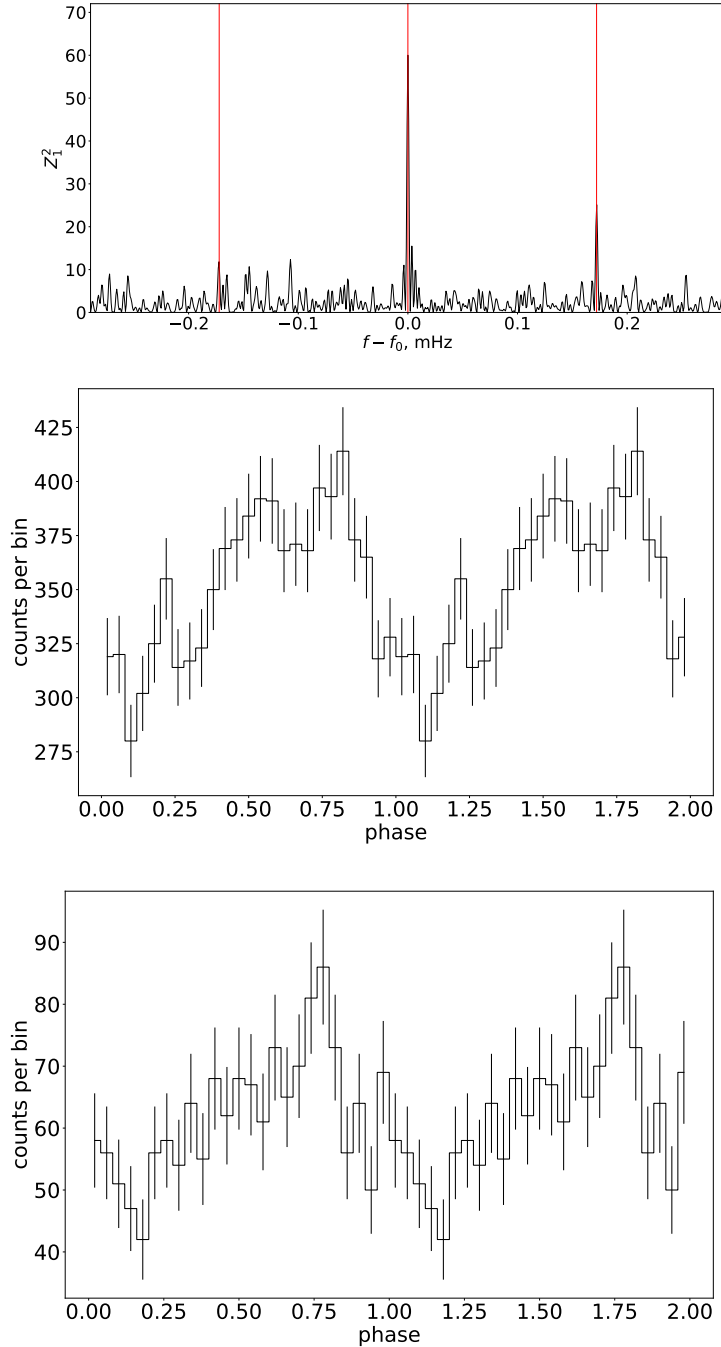


Figure 5. The top panel shows $Z_1^2(f)$ in the vicinity of $f_0 = 0.110498$ Hz ($P_0 = 9.04996$ s) calculated for the entire observation with arrival times corrected for the orbital motion with the same ephemeris as in Figure 4. The vertical red lines mark the aliases of the main peak which are offset from f_0 by ± 0.017 mHz, which is the frequency of the *NuSTAR* orbit around the Earth. The middle and bottom panels show the pulse profiles folded on the period P_0 for the entire observation and for the 270–320 ks interval (counting from the beginning of the observation), where the signal is particularly strong (see Figure 4).

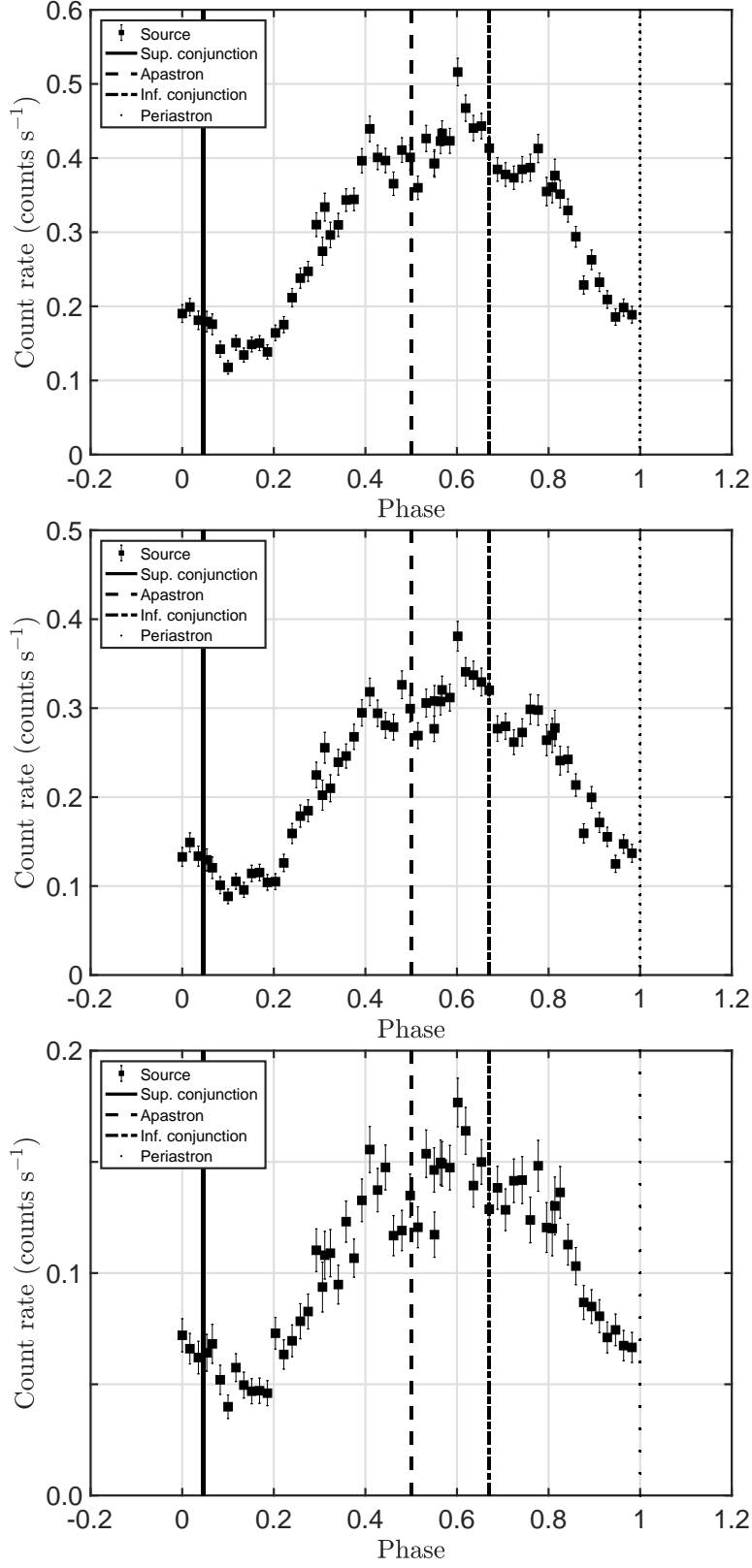


Figure 6. *NuSTAR* background-corrected light curves of LS 5039 as functions of orbital phase. The upper, middle, and lower panels are for the energy bands 3–60 keV, 3–10 keV, and 10–60 keV. The superior and inferior conjunctions are shown by the solid and dash-dot lines, while the apastron and periastron are shown by dashed and dotted lines, respectively.

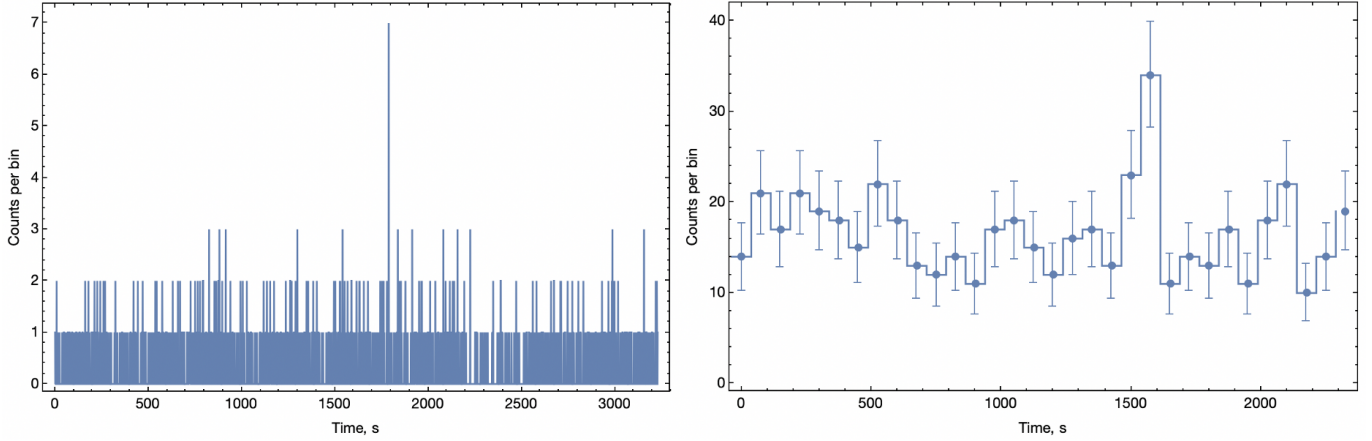


Figure 7. Light curves of the two most significant bursts (3.6σ and 3.2σ , respectively). Bin sizes in the left and right light curves are 1 s and 75 s, respectively. Time (in seconds) is counted from the end of the nearest preceding occultation of the target by Earth.

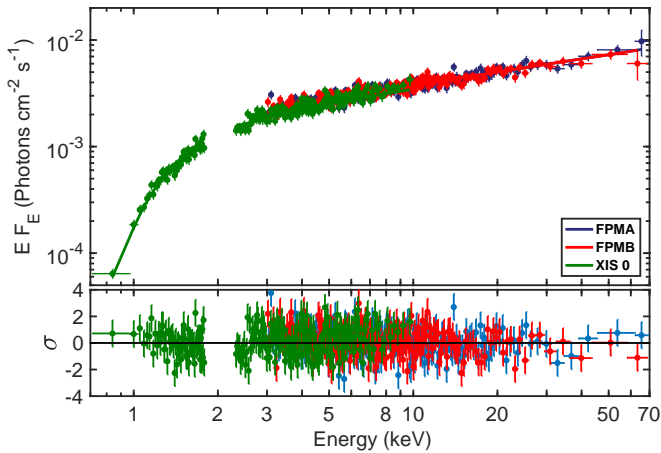


Figure 8. Fit of the absorbed PL model to the phase-integrated *NuSTAR* and *Suzaku* XIS data (for clarity we only show XIS0), and the corresponding residuals in units of σ (lower panel).

where erf^{-1} is the inverse of the error function, $\text{erf}(x) = 2\pi^{-1/2} \int_0^x e^{-z^2} dz$. The value of α_n for a peak in the Fourier power spectrum determines the significance “in units of σ ” of possible detection of a periodic signal with the frequency $n \Delta f$.

The top panel of Figure 2 does not show highly significant peaks, except for those caused by the orbital motion of the *NuSTAR* satellite (at the frequency 1.72×10^{-4} Hz and its harmonics). The visual impression of growing \mathcal{P}_n toward higher frequencies is due to the logarithmic scale – the number of (statistically independent) frequency bins per given log-frequency interval grows with f . The lack of significant detection may be caused by a spread of the signal over several frequency bins due to inaccurate values of the binary parameters (see Appendix B).

In addition to the Fourier spectrum for the entire *NuSTAR* observation, we also calculated 60 power spectra for separate (consecutive) *NuSTAR* orbits (i.e., a dynamical 2D Fourier power spectrum), with average values of 3154 s for the visibility interval, $\Delta f = 3.4 \times 10^{-4}$ Hz for frequency resolution, and $N = 944$ for the number of events per interval. The Römer delay correction was applied before calculating the spectra. Although the individual spectra contain less counts than the spectrum for the entire observation, they are less prone to the loss of coherence caused by the uncertainties of orbital parameters. If signal frequencies are found in each of the 60 time intervals, their dependence

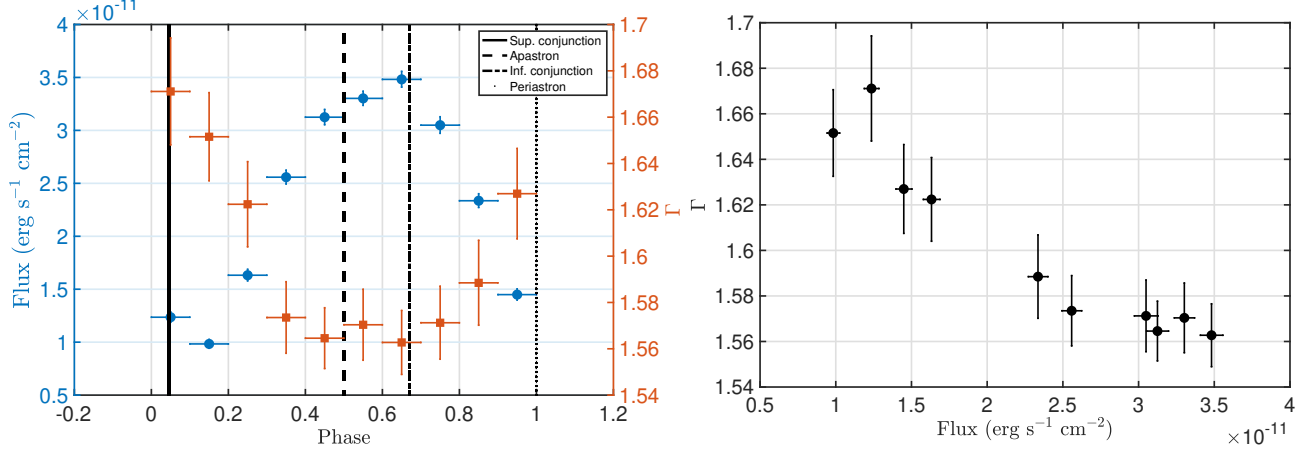


Figure 9. *Left:* Phase-resolved spectroscopic results with $\Delta\phi = 0.1$. The blue points show the 3–70 keV unabsorbed flux variation as a function of orbital phase, with periastron at $\phi = 0$. The orange squares show the photon index variation with phase. *Right:* Anti-correlation of the photon index and the flux.

on interval number (time) would allow one to measure the time-dependent Doppler shift due to the difference between the best-fit and actual binary parameters, and to additionally constrain the binary parameters.

Similar to the 1D spectrum for the entire observation, the Fourier power spectrum of white noise appears to increase toward higher frequencies when plotted on a logarithmic frequency scale. To alleviate this issue, we split the frequency range into K segments of equal size on the logarithmic scale. We chose $K = 200$ for visual clarity. The k -th ($k = 1, \dots, K$) segment contains n_k original frequency bins, and this number grows with k . Within each frequency segment we identified the largest value of Fourier power, \mathcal{P}_k^{\max} (shown in Figure 2, bottom left). Similar to the 1D power spectrum, the probability of getting at least one value $\mathcal{P} > \mathcal{P}_k^{\max}$ within segment k is

$$\Pr(\mathcal{P} > \mathcal{P}_k^{\max}) = 1 - \mathcal{S}_k, \quad \mathcal{S}_k = \left[\int_0^{\mathcal{P}_k^{\max}} \varphi(x) dx \right]^{n_k} = \left[1 - \exp\left(-\frac{\mathcal{P}_k^{\max}}{2}\right) \right]^{n_k} \quad (\text{A5})$$

Similar to the above, we can characterize the k -th frequency segment by the parameter α_k (significance in units of standard deviation):

$$\alpha_k = \sqrt{2} \operatorname{erf}^{-1} \mathcal{S}_k. \quad (\text{A6})$$

The time-frequency image of α_k is shown in Figure 2 (bottom right); it is independent of the number of bins in the k -th frequency segment. Note that α_k only accounts for the number of trials within the k -th segment but not for the total number of trials available (independent frequency values).

B. SEARCHING FOR A PERIODIC SIGNAL FROM A BINARY COMPANION WHEN BINARY PARAMETERS ARE POORLY KNOWN

There can be two approaches to searching for a periodic signal from a companion in a binary system when the binary parameters are not certain enough. In the first approach one creates a sufficiently dense grid in the multi-dimensional space of binary parameters and calculates the Fourier power spectrum for the entire time series of photon arrival times after correcting them for the R mer delay for all parameter values on the grid. This approach relies on the assumption that, for the correct orbital parameter values, the coherence of the periodic signal is maintained throughout the entire observation. Although straightforward, this approach is extremely expensive computationally if the uncertainties of the binary parameters are as large as they are in the case of LS 5039 (Caliandro et al. 2012). Therefore, we have to resort to a different approach where the observation is divided into time segments and the coherence is maintained only locally within the each time segment.

In the Appendix A and Section 3.2.2, we described the case when the lengths of time segments coincide with the visibility intervals in 60 separate *NuSTAR* orbits. However, it is not necessarily the best possible choice. To choose the optimal number and lengths of time segments, one should take into account the frequency variation due to the Doppler effect.

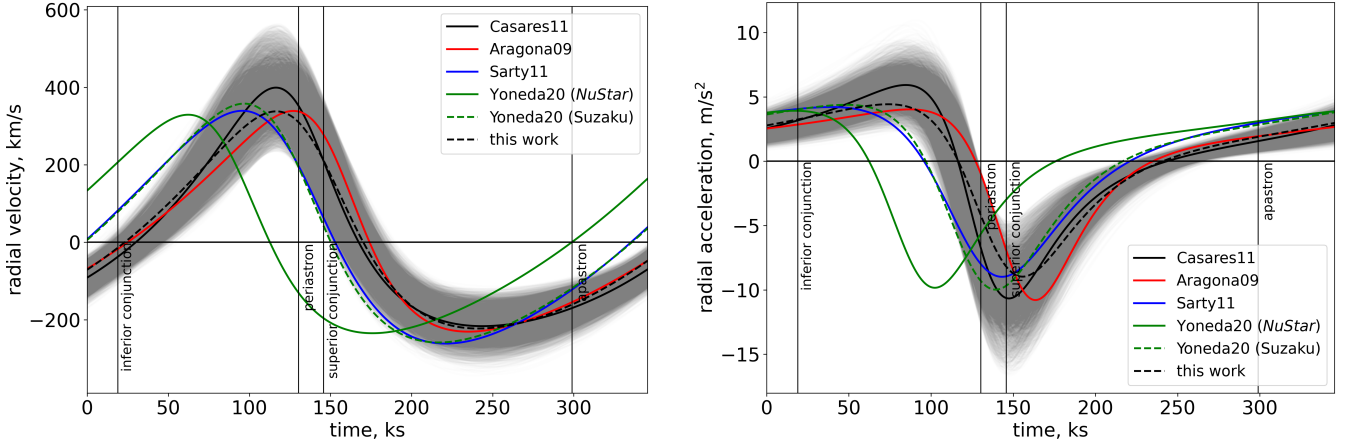


Figure 10. Radial projections of the velocity and acceleration of the compact object during our *NuSTAR* observation for orbital parameters from Aragona et al. (2009), Casares et al. (2011), Sarty et al. (2011), Y+20, and from this work, listed in Table 1. The former 3 curves (black, red and blue) correspond to the optically measured best-fit binary parameters, assuming the compact object mass of $1.8M_{\odot}$ for Casares et al. (2011) and Sarty et al. (2011), and $1.6M_{\odot}$ for Aragona et al. (2009). The solid and dashed green curves correspond to the orbital parameters for which Y+20 claimed the periods $P \approx 9.05$ s and ≈ 8.96 s in the *NuSTAR* and *Suzaku* data, respectively. The black dashed curves correspond to the orbital parameters for which we found the most significant candidate for the $P \approx 9.05$ s period. The shaded areas around the solid black curves demonstrate the uncertainties of radial velocity and acceleration derived from the Casares et al. (2011) parameters.

If we do not apply the Römer delay correction, the observed frequency varies along the orbit as $f(t) = f_0[1 + v_{\parallel}(t)/c]$, where f_0 is the frequency in the reference frame of the source, and $v_{\parallel}(t)$ is the radial velocity of the source of signal (see Figure 10),

$$v_{\parallel}(t) = \Omega_{\text{orb}} \frac{a_p \sin i}{\sqrt{1 - e^2}} [\cos(\theta + W_p) + e \cos W_p], \quad (\text{B7})$$

θ is the true anomaly

$$\theta = 2 \arctan \left(\sqrt{\frac{1+e}{1-e}} \tan \frac{E}{2} \right). \quad (\text{B8})$$

Let us consider the case when the entire observation is split into N_w equal time segments (windows) of duration T_w (i.e., $T_w = T_{\text{obs}}/N_w$), numbered as $j = 1, 2, \dots, N_w$. If $T_w \ll P_{\text{orb}}$ (which implies $N_w \gg 1$ for our case, when $T_{\text{obs}} \approx P_{\text{orb}}$), the radial velocity within the j -th time segment, $t_j - T_w/2 < t < t_j + T_w/2$, varies as $v_{\parallel}(t) \approx v_{\parallel}(t_j) + \dot{v}_{\parallel}(t_j)(t - t_j)$, where $\dot{v}_{\parallel}(t_j)$ is the radial acceleration,

$$\dot{v}_{\parallel}(t) = -\Omega_{\text{orb}}^2 \frac{a_p \sin i}{(1 - e^2)^2} (1 + e \cos \theta)^2 \sin(\theta + W_p), \quad (\text{B9})$$

in the middle of the segment. Thus, the frequency within the j -th time segment varies as $f_j(t) \approx f_0[1 + v_{\parallel}(t_j)/c + \dot{v}_{\parallel}(t_j)(t - t_j)/c]$, where the second term corresponds to the frequency shift in the middle of the j -th segment, and the third term describes the frequency drift within this segment. As $N_w \gg 1$, the maximum drift during the entire segment, $|\dot{v}_{\parallel}(t_j)|T_w f_0/c$, is much smaller than the maximal frequency spread, $(v_{\parallel\text{max}} - v_{\parallel\text{min}})f_0/c$, during the entire observation.

If the orbital parameters were exactly known, then the Römer delay correction would eliminate the frequency spread. However, when the uncertainties are large (as in the case of LS 5039), a residual spread remains even after the correction, which lowers the sensitivity of the pulsation search if the time segments are too wide. In the case of $N_w \gg 1$ this spread is determined by the uncertainty of the radial acceleration.

In order to determine this uncertainty, we created $N_{\text{orb}} = 1000$ orbits by random sampling from the multivariate Gaussian probability distribution of the orbital parameters with means and standard deviations listed in Table 1. For each orbit we calculated the mean-square deviation of the radial acceleration $\dot{v}_{\parallel,i}(t)$ from the most likely value, $\dot{v}_{\parallel,0}(t)$,

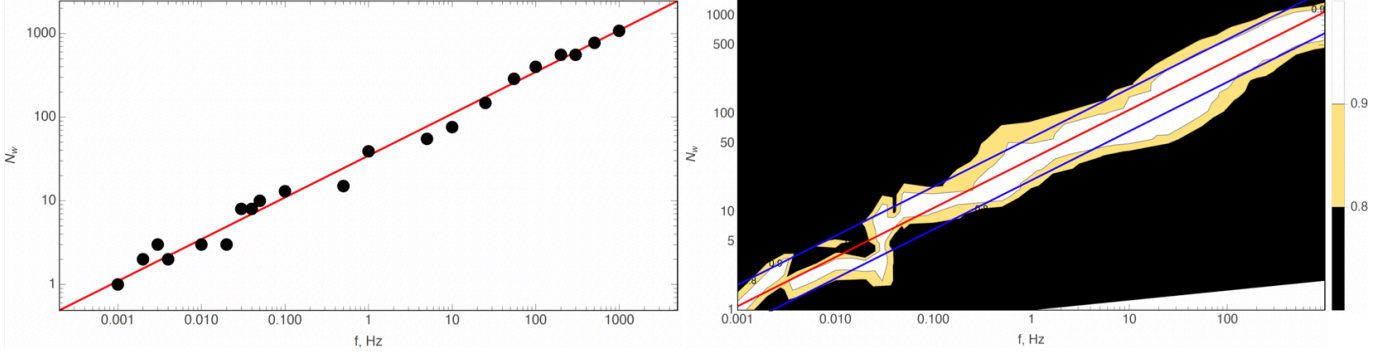


Figure 11. Optimal number of time segments N_w vs. frequency f . Left panel: Dots show the results of MC simulations; the red line is a fit $N_w = 34.66f^{1/2}$ (which corresponds to effective acceleration uncertainty of 3 m s^{-2} ; cf. Figure 10, right). Right panel: Contour plot showing the areas where the deviations from optimal N_w lead to the signal power being reduced by 10% and 20% (shown by color). We chose such N_w values so that for each frequency the signal power lies between the two blue lines.

corresponding to the orbit with the best-fit orbital parameters (Table 1):

$$d_i = \frac{1}{T_{\text{obs}}} \int_0^{T_{\text{obs}}} [\dot{v}_{\parallel,i}(t) - \dot{v}_{\parallel,0}(t)]^2 dt. \quad (\text{B10})$$

We then constructed a probability distribution function of the deviations, $p_{d,i}$, which appear to be log-normally distributed. Then the radial acceleration uncertainty (standard deviation) can be estimated as

$$\delta \dot{v}_{\parallel}(t) = \left\{ \sum_{i=1}^{N_{\text{orb}}} [\dot{v}_{\parallel,i}(t) - \dot{v}_{\parallel,0}(t)]^2 p_{d,i} \right\}^{1/2}. \quad (\text{B11})$$

The uncertainties of radial velocity and Römer delay were estimated in a similar manner. The uncertainties are shown as shaded areas in Figures 1 and 10.

Since the radial acceleration uncertainty does not change substantially throughout the orbit, we can replace $\delta \dot{v}_{\parallel}(t_j)$ by an ‘effective radial acceleration’ a_{eff} . The frequency spread caused by the radial acceleration uncertainty, $\sim f a_{\text{eff}} T_w / c$, is equal to the width of the frequency bin, T_w^{-1} , in the Fourier spectrum if

$$N_w \sim T_{\text{obs}} (f a_{\text{eff}} / c)^{1/2}. \quad (\text{B12})$$

Dividing into more segments would reduce the signal strength because the Fourier power is proportional to the number of events and hence to T_w . Therefore, this N_w represents the optimal split into time segments of equal lengths.

In order to evaluate a_{eff} for our data, we performed a Monte-Carlo search by generating periodic signals at various frequencies, applying a partial Römer correction, and finding such N_w that maximizes the signal’s power in a time segment (see Figure 11). We found that the dependence of N_w on frequency follows Equation (B12) most closely for $a_{\text{eff}} \approx 3 \text{ m s}^{-2}$, comparable with the acceleration uncertainty (see Figure 10, right panel), i.e., the optimal number and lengths of time segments can be estimated as $N_w \sim 35f^{1/2}$ and $T_w \sim 9.9f^{-1/2} \text{ ks}$ in our case.

For the actual period search, it is convenient to specify a few frequency intervals with different optimal N_w numbers for each of them. Based on the simulations, we selected 7 different sets of subdivisions of the entire T_{obs} into smaller segments, such that for any frequency f the signal deteriorates by at most 10%: $N_w = 1$ for $f < 0.017 \text{ Hz}$, $N_w = 7$ for $0.017 \leq f < 0.124$, $N_w = 20$ for $0.124 \leq f < 0.912$, $N_w = 55$ for $0.913 \leq f < 6.74$, $N_w = 148$ for $6.74 \leq f < 49.8$, $N_w = 403$ for $49.8 \leq f < 368$, and $N_w = 854$ for $f \geq 368 \text{ Hz}$.

Examples of simulated dynamic Fourier power spectra in the time-frequency domain (time in units of orbital phase) are shown in Figure 12 for sinusoidal pulsations with the intrinsic frequencies $f_0 = 1, 10$ and 100 Hz and various pulsed fractions p (defined as the ratio of the number of signal events to the total number of events).

In order to detect the signal in the dynamic Fourier power spectrum, we split the entire frequency range into segments that are wide enough to ensure that they contain the entire signal (i.e., the entire $f(\phi)$ curves, similar to those in Figure 12, are within these frequency segments). The half-width of a frequency segment can be estimated as $\delta f = \beta f_0$.

The coefficient β is proportional to $\delta v_{\parallel}/c$, where δv_{\parallel} is the maximum amplitude of the residual uncertainties of radial velocity. The Monte Carlo (MC) simulations show that δv_{\parallel} exceeds 300 km s^{-1} (i.e., $\delta v_{\parallel}/c > 10^{-3}$) in only $\approx 1\%$ of simulations. To increase the chances to capture a signal in a single frequency segment, we conservatively chose $\beta = 2.2 \times 10^{-3}$. For a time window of width T_w , the number of frequency resolution bins within such a frequency segment around a central frequency f_0 is $N_f = 2\beta f_0 T_w$.

The dependence of the central frequency f_m of a segment on its number m follows from the relationship $f_m + \beta f_m = f_{m+1} - \beta f_{m+1}$:

$$f_m = \left(\frac{1+\beta}{1-\beta} \right)^{m-1} f_1, \quad (\text{B13})$$

where f_1 is the central frequency of the first segment within some frequency interval. The total number of frequency segments in the range (f_{\min}, f_{\max}) can be estimated as

$$m_{\max} \approx 1 + \frac{1}{2\beta} \ln \frac{f_{\max}}{f_{\min}}. \quad (\text{B14})$$

For instance, $m_{\max} \approx 2500$ for $f_{\max} = 1000 \text{ Hz}$, $f_{\min} = 0.017 \text{ Hz}$, $\beta = 2.2 \cdot 10^{-3}$.

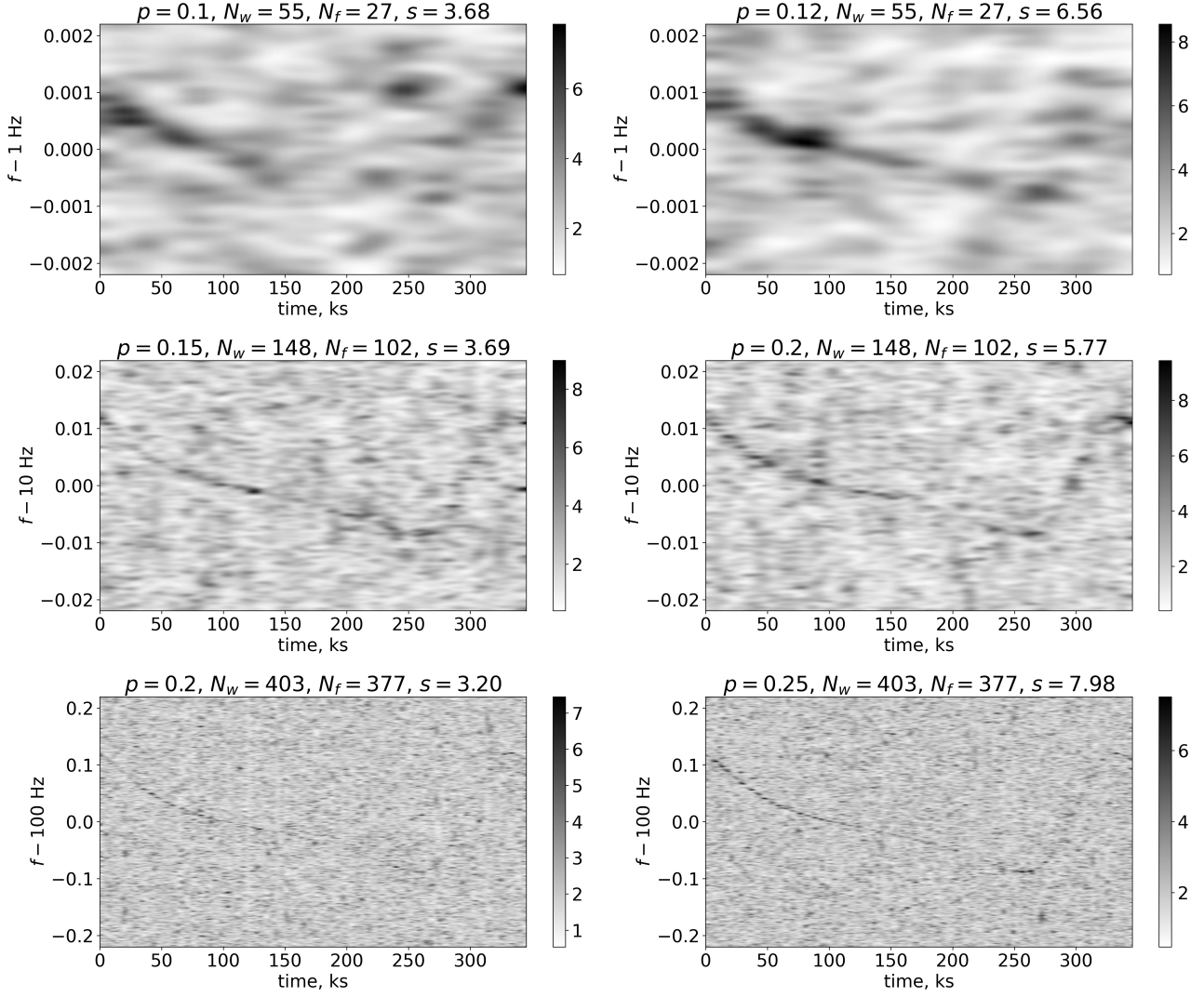


Figure 12. Images in the time-frequency plane of the Fourier power for artificial periodic signals after imperfect (due to the imprecisely known ephemeris) Römer delay correction for 3 signal frequencies and several pulsed fractions p . Each image has $N_w \times 5N_f$ ‘pixels’, where N_w is the number of time (orbital phase) windows, and N_f is the number of frequency segments (we used the frequency step $(5T_w)^{-1}$ for greater sensitivity and visual clarity). We have applied a Gaussian blur to make the periodic signal visible by eye. Color bars indicate the magnitude of the Fourier power \mathcal{P}_n , defined in Equation (A1). On top of each plot we show the corresponding value of the s -statistic, defined in Section 3.2.3. In all the simulations we assumed that the binary has the following ‘true’ orbital parameters: $\{a_p \sin i = 51.7$ lt-s, $e = 0.35$, $T_0 = 52477.58$ MJD, $P_{\text{orb}} = 3.90608$ d, and $W_p = 32^\circ\}$ but applied the Römer delay correction using a different set: $\{a_p \sin i = 45.2$ lt-s, $e = 0.33$, $T_0 = 52477.55$ MJD, $P_{\text{orb}} = 3.90604$ d, and $W_p = 29.5^\circ\}$.

REFERENCES

- An, H., Dufour, F., Kaspi, V. M., et al. 2013, *ApJ*, 775, 135
- An, H., Bellm, E., Bhalerao, V., et al. 2015, *ApJ*, 806, 166
- Aragona, C., McSwain, M. V., Grundstrom, E. D., et al. 2009, *ApJ*, 698, 514
- Archer, A., Benbow, W., Bird, R., et al. 2020, *ApJ*, 888, 115
- Arnaud, K. A. 1996, *Astronomical Data Analysis Software and Systems V*, 101, 17
- Bachetti, M., Markwardt, C. B., Grefenstette, B. W., et al. 2021, *ApJ*, 908, 184
- Blandford, R. & Teukolsky, S. A. 1976, *ApJ*, 205, 580
- Bogovalov, S. V., Khangulyan, D., Koldoba, A. V., et al. 2012, *MNRAS*, 419, 3426
- Bogovalov, S. V., Khangulyan, D., Koldoba, A., et al. 2019, *MNRAS*, 490, 3601
- Bosch-Ramon, V., Paredes, J. M., Ribó, M., et al. 2005, *ApJ*, 628, 388. doi:10.1086/429901
- Buccheri, R., Bennett, K., Bignami, G. F., et al. 1983, *A&A*, 128, 245
- Caliandro, G. A., Torres, D. F., & N. Rea, N. 2012, *MNRAS*, 427, 2251
- Camilo, F., Ray, P. S., Ransom, S. M., et al. 2009, *ApJ*, 705, 1
- Casares, J., Ribó, M., Ribas, I., et al. 2005, *MNRAS*, 364, 899
- Casares, J. et al. 2011, *New Optical Results on γ -ray Binaries. In High-Energy Emission from Pulsars and their Systems*, Springer, Astrophysics and Space Science Proceedings, 21, 559
- Chernyakova, M., Neronov, A., van Soelen, B., et al. 2015, *MNRAS*, 454, 1358. doi:10.1093/mnras/stv1988
- Coburn, W., Heindl, W. A., Rothschild, R. E., et al. 2002, *ApJ*, 580, 394. doi:10.1086/343033
- Coley, J. B., Boyd, P., Corbet, R. H. D., et al. 2020, *American Astronomical Society Meeting Abstracts*
- de Jager, O. C., Raubenheimer, B. C., & Swanepoel, J. W. H. 1989, *A&A*, 221, 180
- Dubus, G. 2006, *A&A*, 456, 801
- Dubus, G. 2013, *A&A Rv*, 21, 64
- Dubus, G. 2015, *Comptes Rendus Physique*, 16, 661
- Fornasini, F. M., Tomsick, J. A., Bachetti, M., et al. 2017, *ApJ*, 841, 35. doi:10.3847/1538-4357/aa6ff4
- Fürst, F., Pottschmidt, K., Wilms, J., et al. 2014, *ApJL*, 784, L40
- Harrison, F. A., Craig, W. W., Christensen, F. E., et al. 2013, *ApJ*, 770, 103. doi:10.1088/0004-637X/770/2/103
- Kargaltsev, O., & Pavlov, G. G. 2008, *40 Years of Pulsars: Millisecond Pulsars, Magnetars and More*, AIP Conference Proceedings, 983, 171
- Kargaltsev, O., Rangelov, B., Hare, J., et al. 2014, *Astronomische Nachrichten*, 335, 301
- Kaspi, V. M. & Beloborodov, A. M. 2017, *ARA&A*, 55, 261
- Kishishita, T., Tanaka, T., Uchiyama, Y., et al. 2009, *ApJL*, 697, L1. doi:10.1088/0004-637X/697/1/L1
- Koyama, K., Tsunemi, H., Dotani, T., et al. 2007, *PASJ*, 59, 23.
- Krivonos, R. A., Tsygankov, S. S., Lutovinov, A. A., et al. 2015, *ApJ*, 809, 140. doi:10.1088/0004-637X/809/2/140
- Li, K. L., Kong, A. K. H., Tam, P. H. T., et al. 2017, *ApJ*, 843, 85. doi:10.3847/1538-4357/aa784e
- Lohfink, A. M., Reynolds, C. S., Jorstad, S. G., et al. 2013, *ApJ*, 772, 83. doi:10.1088/0004-637X/772/2/83
- Lorimer, D. R. & Kramer, M. 2012, *Handbook of Pulsar Astronomy*, by D. R. Lorimer, M. Kramer, Cambridge, UK: Cambridge University Press, 2012
- Marti, J., Paredes, J. M., & Ribo, M. 1998, *A&A*, 338, L71
- Massi, M., Migliari, S., & Chernyakova, M. 2017, *MNRAS*, 468, 3689
- Massi, M., Chernyakova, M., Kraus, A., et al. 2020, *MNRAS*, 498, 3592
- Moldón, J., Ribó, M., & Paredes, J. M. 2012, *A&A*, 548, A103
- Molina, E. & Bosch-Ramon, V. 2020, *A&A*, 641, A84
- Paredes, J. M., Martí, J., Ribó, M., et al. 2000, *Science*, 288, 2340
- Paredes, J. M., & Bordas, P. 2019, *arXiv e-prints*, arXiv:1901.03624
- Prado, R. R., Hailey, C., Mandel, S., et al. 2019, *arXiv:1908.03083*
- Ransom, S. M., Eikenberry, S. S. & Middleditch, J. 2002, *AJ*, 124, 1788.
- Rea, N., Torres, D. F., Caliandro, G. A., et al. 2011, *MNRAS*, 416, 1514
- Rieger, F. M. & Duffy, P. 2016, *ApJ*, 833, 34. doi:10.3847/1538-4357/833/1/34
- Sarty, G. E., Szalai, T., Kiss, L. L., et al. 2011, *MNRAS*, 411, 1293
- Sato, T., Matsushita, K., Ota, N., et al. 2011, *PASJ*, 63, S991. doi:10.1093/pasj/63.sp3.S991
- Serlemitsos, P. J., Soong, Y., Chan, K.-W., et al. 2007, *PASJ*, 59, S9.
- Shannon, R. M., Johnston, S., & Manchester, R. N. 2014, *MNRAS*, 437, 3255
- Takahashi, T., Kishishita, T., Uchiyama, Y., et al. 2009, *ApJ*, 697, 592.
- Torres, D. F., Rea, N., Esposito, P., et al. 2012, *ApJ*, 744, 106

Tsygankov, S. S., Lutovinov, A. A., Krivonos, R. A., et al.
2016, MNRAS, 457, 258
Verner, D. A., Verner, E. M., & Ferland, G. J. 1996,
Atomic Data and Nuclear Data Tables, 64, 1

Wilms, J., Allen, A., & McCray, R. 2000, ApJ, 542, 914
Yoneda, H., Makishima, K., Enoto, T., et al. 2020, PRL,
125, 111103, (Y+20)